


Cite this: *RSC Adv.*, 2021, 11, 4723

# Three-dimensional graphene encapsulated Ag–ZnFe<sub>2</sub>O<sub>4</sub> flower-like nanocomposites with enhanced photocatalytic degradation of enrofloxacin†

Kangwang Wang,<sup>a</sup> Sheng Zhan,<sup>b</sup> Danyang Zhang,<sup>c</sup> Hui Sun,<sup>b</sup> Xiaodong Jin<sup>a</sup> and Juan Wang<sup>id</sup>\*<sup>cd</sup>

Three-dimensional (3D) Ag–ZnFe<sub>2</sub>O<sub>4</sub>-reduced graphene oxide (rGO) was successfully synthesized using a hydrothermal and photo-reduction method, and the morphological differences of the materials were observed. Their photocatalytic activity was evaluated by photocatalytic degradation of enrofloxacin (ENR) under visible-light irradiation. The results indicated that Ag–ZnFe<sub>2</sub>O<sub>4</sub>-rGO exhibited superior photocatalytic properties and good stability. In this research, the enhancement of photocatalytic performance is mainly attributed to the electron channelization ability of rGO, which traps the photoexcited electrons of ZnFe<sub>2</sub>O<sub>4</sub> on its  $\pi$  framework, and reduces the electron–hole recombination rate. Moreover, the high surface area of 3D pompon mum flower-like ZnFe<sub>2</sub>O<sub>4</sub> provides more reactive sites. In addition, free radical capture and ESR experiments as well as pathway analysis of degradation also confirmed that superoxide radicals ( $\cdot\text{O}_2^-$ ) and photo-generated holes from Ag–ZnFe<sub>2</sub>O<sub>4</sub>-rGO were the main active species in the degradation progress of ENR.

Received 11th November 2020  
Accepted 19th January 2021

DOI: 10.1039/d0ra09582f

rsc.li/rsc-advances

## 1. Introduction

Different environmental pollution includes soil, air, water, heat, noise and light pollutions, and water pollution is among the main environmental challenge confronted by society. Nowadays, with society and information technology developing, the degradation of organic contaminants has been investigated using various techniques and systems. There is no doubt that organic contaminants will, directly or indirectly, have a great influence on our academic studies.<sup>1–4</sup> Enrofloxacin (ENR), as a representative of fluoroquinolones, is widely used to treat various infections in animals. Traditional sewage treatment cannot effectively eliminate excess antibiotics, so that ENR is often detected in various water environments.<sup>5</sup> Consequently, it is imperative for us to develop a highly efficient steady strategy to degrade subaqueous ENR. As is known to us all, photocatalytic materials can effectively convert solar energy into

chemical energy to degrade water and air contaminants, which is of great significance for addressing environmental pollution issues in modern society. Given the serious energy crisis, semiconductor photocatalysis can be a promising technology for the complete elimination of various contaminants.<sup>6</sup> In the frontier area of catalysis, it is currently a hot topic that plasmonic photocatalysts characterized by distinct surface plasmon resonance (SPR) absorptions over a wide range of visible-light regions are promising materials as high-performance visible-light-energized photocatalysts. Until now, spinel ZnFe<sub>2</sub>O<sub>4</sub> has drawn broad attention due to its narrow band gap of approximately 1.9 eV, which can be excited by visible-light and ability to utilize sunlight. In addition, ZnFe<sub>2</sub>O<sub>4</sub> works as a photocatalyst that has been widely evaluated in remediation of polluted environmental because of its excellent photoelectricity transformation ability and photosensitive effect. However, the low separation rate and high recombination rate of photo-generated electrons ( $e^-$ ) and holes ( $h^+$ ) can largely obstruct applications.<sup>7,8</sup> Therefore, some co-catalysts are introduced into the photocatalytic system to improve the separation efficiency of photo-generated  $e^-/h^+$  pairs. The photocatalytic activity of the catalyst was improved by reducing the photo-generated  $e^-/h^+$  pair recombination rate.<sup>9</sup> Carbon materials such as graphene and carbon nanotubes have been used as co-catalyst materials.<sup>10,11</sup> Ag nanoparticles (Ag NPs), as facile and efficient light absorbers, were often modified on the surface of ZnFe<sub>2</sub>O<sub>4</sub>, which exhibit enhanced photocatalytic performance against

<sup>a</sup>School of Chemical and Biological Engineering, Lanzhou Jiaotong University, Lanzhou, 730070, P. R. China

<sup>b</sup>School of Materials Science and Engineering, Shaanxi Normal University, Xi'an, 710119, P. R. China

<sup>c</sup>School of Chemistry and Chemical Engineering, Shaanxi Normal University, Xi'an, 710062, P. R. China. E-mail: wangvipjuan@163.com

<sup>d</sup>School of Medicine, Shaanxi Institute of International Trade & Commerce, Xi'an, 712046, P. R. China

† Electronic supplementary information (ESI) available. See DOI: 10.1039/d0ra09582f



bacterial infection. Nevertheless, the high cytotoxicity of  $\text{Ag}^+$  released from Ag NPs severely limited the application of hybrid  $\text{ZnFe}_2\text{O}_4/\text{Ag}$  NPs based antibacterial materials in the biomedical field.<sup>12,13</sup>

Graphene oxide (GO), a honeycomb and one-atom-thick structured carbon material, whose basal plane and edge are decorated with abundant oxygen-containing functional groups (e.g.,  $-\text{OH}$ ,  $-\text{COOH}$ ,  $\text{C}=\text{O}$ ,  $-\text{CH}(\text{O})\text{CH}^-$ ), has been verified to be an excellent catalyst carrier and promoter.<sup>14</sup> Due to its unique structure and excellent electronic, electrochemical, optical, thermal and mechanical properties, GO has already been possessed broad application prospects. Simultaneously, GO has a large specific surface area, a high electron transfer efficiency, and excellent adsorption.<sup>15</sup> Taking the above highlighted advantageous features into account many metal oxide-GO based nanocomposites were fabricated with increase visible-light absorptivity and longer lifespan of exciton pairs.<sup>16</sup> Generally, sole semiconductor photocatalyst demonstrates poor photocatalytic performance due to the rapid recombination of photogenerated charge carriers and low quantum efficiency. Heterojunction formation is an efficient way to extend the visible light absorption range and accelerate the charge separation.<sup>17</sup> In this regard, a few researchers have studied this area in detail and many semiconductors such as  $\text{ZnFe}_2\text{O}_4\text{-Ag/rGO}$ ,<sup>18</sup>  $\text{H-PPAN/rGO-g-PAO@Ag}^+/\text{Ag}$ ,<sup>19</sup>  $\text{rGO-MFe}_2\text{O}_4$  ( $\text{M} = \text{Ni}$ ,  $\text{Co}$ , and  $\text{Zn}$ ),<sup>20</sup>  $\text{Ag-ZnFe}_2\text{O}_4\text{@rGO}$ ,<sup>21</sup>  $\text{ZnFe}_2\text{O}_4\text{@graphene}$ <sup>22</sup> and  $\text{ZnFe}_2\text{O}_4/\text{RGO/In}_2\text{O}_3$  (ref. 23) have been effectively synthesized. Nanocomposites containing magnetic materials are highly advantageous as they can be easily be separated from the medium. In this regard, Jiang *et al.* synthesized graphene- $\text{WO}_3$  nanocomposites, exhibits the highest catalytic performance and the corresponding removal efficiency can reach 99.1% with 60 min treatment time.<sup>24</sup> Wang *et al.* after the introduction of graphene in Au NPs-PtDPAP/CdS, the degradation efficiency on TC was further improved (90% in 3 h).<sup>25</sup> In addition, both  $\text{ZnFe}_2\text{O}_4$  and  $\text{ZnFe}_2\text{O}_4$ -based composites such as  $\text{ZnFe}_2\text{O}_4$ -reduced graphene oxide hybrid can act as photo-Fenton-like catalysts to improve the degradation rate of organic antibiotics under visible-light irradiation in the presence of  $\text{H}_2\text{O}_2$ .<sup>26</sup> In recent years, in order to treat wastewaters that contain these kinds of pharmaceuticals which cannot be degraded biologically, Advanced Oxidation Processes (AOPs) gain attention. AOPs which do not require high temperature and pressure, produce reactive radicals ( $\cdot\text{OH}$ ,  $\cdot\text{O}_2^-$ ) at medium conditions. Formed radicals oxidize organic antibiotics to convert them to  $\text{CO}_2$  and  $\text{H}_2\text{O}$ . Thus, the photocatalytic oxidation which is the one of AOPs was used in to degrade enrofloxacin (ENR) under visible-light illumination.<sup>27</sup> Photocatalytic oxidation (photocatalysis) can be declared as acceleration of a photoreaction by presence of a proper photocatalyst.

In this contribution, a novel 3D separable and recyclable  $\text{Ag-ZnFe}_2\text{O}_4\text{-rGO}$  photocatalyst with the pompon mum flower-like and photocatalytic degradation was successfully prepared *via* a facile hydrothermal, and heat treatment, as well photo-reduction method. The graphene oxide (GO) was reduced to the reduced graphene oxides (rGO) and covered on the surface of the  $\text{ZnFe}_2\text{O}_4$  nanoflowers. Ag NPs were deposited *in situ* on

rGO by photo-reduction  $\text{Ag}^+$  to form the  $\text{Ag-ZnFe}_2\text{O}_4\text{-rGO}$  composites. The synthesized exhibited high photocatalytic activity on the degradation of the ENR under visible-light irradiation. The magnetic properties of  $\text{ZnFe}_2\text{O}_4$  could make the separation of the nanocomposite easier, avoiding environmental contamination from processing. Moreover, the nanocomposites represented high photocatalytic stability and reusability. The photocatalytic properties of  $\text{Ag-ZnFe}_2\text{O}_4\text{-rGO}$  for antibiotic degradation were discussed under visible-light irradiation, and the structure-activity relationship between electronic structure, and photocatalytic activity were also studied. In addition, a reasonable photocatalytic mechanism for the degradation of antibiotics was also explained in detail. Simultaneously, we explored the conversion pathway of ENR in the photocatalytic degradation process.

## 2. Experimental section

### 2.1 Synthesis of 3D $\text{ZnFe}_2\text{O}_4$ pompon mum nanoflowers

3D  $\text{ZnFe}_2\text{O}_4$  nanoflowers have been synthesized through a simple hydrothermal method using  $\text{ZnCl}_2$  and  $\text{FeCl}_3 \cdot 6\text{H}_2\text{O}$  as Zn and Fe sources, respectively. Firstly, in a typical synthesis procedure,  $\text{FeCl}_3 \cdot 6\text{H}_2\text{O}$  (1.08 g, 4.0 mmol),  $\text{ZnCl}_2$  (0.27 g, 2.0 mmol) were dissolved in ethylene glycol (40 mL), and then transferred to a Teflon-lined stainless-steel autoclave (50 mL). The autoclave was kept at 180 °C for 30 min under Ar flow. Secondly, the urea (0.60 g, 10.0 mmol) was added into above solution quickly. After continuously mechanical stirring at 200 °C for 2 h, the yellow precursor precipitate ( $\text{ZnFe}$ -alkoxide precursor) was collected by centrifugation, and washed with absolute ethanol and deionized water, repeatedly. Finally, the precursor was further annealed at 450 °C in  $\text{N}_2$  for 3 h with a relatively slow heating rate of 5 °C  $\text{min}^{-1}$  to obtain 3D  $\text{ZnFe}_2\text{O}_4$  nanoflowers.

### 2.2 Synthesis of the $\text{ZnFe}_2\text{O}_4\text{-rGO}$ nanocomposites

In the following step,  $\text{ZnFe}_2\text{O}_4\text{-rGO}$  was synthesized as follows: 0.1 g of the as-obtained  $\text{ZnFe}_2\text{O}_4$  nanoflowers was dispersed into 20 mL of deionized water under vigorous agitation, followed by adding 25 mL of GO solution (1.0 mg  $\text{mL}^{-1}$ ), stirring for 30 min and then adding 10 mL of CTAB (0.5 mg  $\text{mL}^{-1}$ ) solution to produce graphene oxides encapsulated  $\text{ZnFe}_2\text{O}_4\text{-rGO}$  composites. Graphene oxides would be reduced to the rGO during the subsequently annealing treatment of the  $\text{ZnFe}_2\text{O}_4\text{-GO}$  at 500 °C for 2 h in Ar, and finally 3D graphene encapsulated  $\text{ZnFe}_2\text{O}_4\text{-rGO}$  composites could be harvested. It was cooled naturally, solid separated, washed with ethanol and Milli-Q water, repeatedly, dried at 65 °C (for 12 h).

### 2.3 Synthesis of the $\text{Ag-ZnFe}_2\text{O}_4\text{-rGO}$ nanocomposites

Ag NPs were embedded on the as-acquired 3D  $\text{ZnFe}_2\text{O}_4\text{-rGO}$  nanoflowers through photo-irradiation reduction by  $\text{Ag}^+$  ions. In particular, solid  $\text{AgNO}_3$  (10.0 mg) and methanol (2.0 mL) solution were added to the obtained aqueous suspension (0.5 g, 25 mL) of the  $\text{ZnFe}_2\text{O}_4\text{-rGO}$  nanocomposite, and 100 W mercury lamp was irradiated at  $\lambda = 365$  nm for 5 h. The black solid ( $\text{Ag-}$



ZnFe<sub>2</sub>O<sub>4</sub>-rGO) was separated by an external magnet and washed with Milli-Q water and ethanol, repeatedly, and then dried at 120 °C for 2 h. In the result and discussion section, the inlay situation of Ag NPs is analyzed and discussed in detail. Fig. S1† presents the proposed formation process of the Ag-ZnFe<sub>2</sub>O<sub>4</sub>-rGO nanocomposites.

## 2.4 Photocatalytic activity measurement

The photocatalytic degradation activity of the as-acquired Ag-ZnFe<sub>2</sub>O<sub>4</sub>-rGO photocatalysts was evaluated by the photocatalytic degradation of ENR under visible-light irradiation. First of all, a 300 W Xe lamp with a UV cutoff filter ( $\lambda > 400$  nm) was used as the visible-light source ( $\lambda = 465$  nm) in the photocatalytic degradation reaction. Briefly, the Ag-ZnFe<sub>2</sub>O<sub>4</sub>-rGO (15 mg) was dispersed in 50 mL of an aqueous ENR solution (10 mg L<sup>-1</sup>) in this work. Then, the photocatalyst was fully in contact with ENR molecules to ensure the adsorption-

desorption equilibrium by shaking them for 15 min using a blender in the dark. Moreover, at predetermined time intervals (5 min), 3.0 mL of liquid was drawn from the degradation reaction solution, and the supernatant was extracted by centrifugation (10 000 rpm, 20 min). In addition, the photocatalytic degradation reaction is degraded in the degradation tank at room temperature. Finally, the residual concentrations of ENR in the reaction solution were detected by UV-vis spectrophotometry at  $\lambda = 271$ .

The photodegradation efficiency ( $\eta_{\text{eff}}$ ) of the ENR solution was determined according to the following eqn (1):<sup>21</sup>

$$\eta_{\text{eff}} = \left(1 - \frac{C_t}{C_0}\right) \times 100\% = \left(1 - \frac{A_t}{A_0}\right) \times 100\% \quad (1)$$

where  $A_0$  and  $C_0$  are the absorbance and concentration of the pure antibiotic solution (mg L<sup>-1</sup>),  $A_t$  and  $C_t$  are the absorbance and the concentration of ENR at a given reaction time (mg L<sup>-1</sup>).

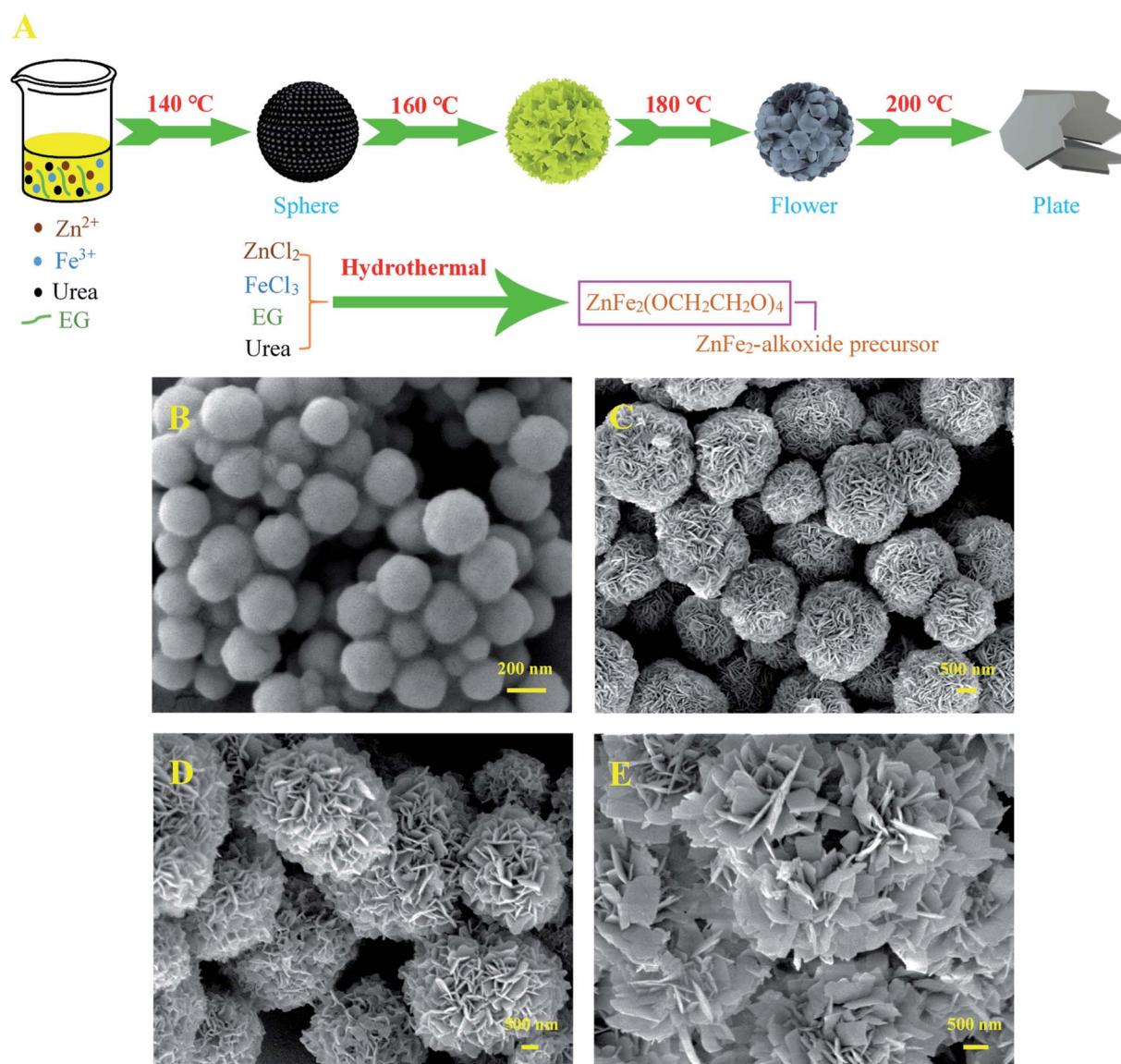
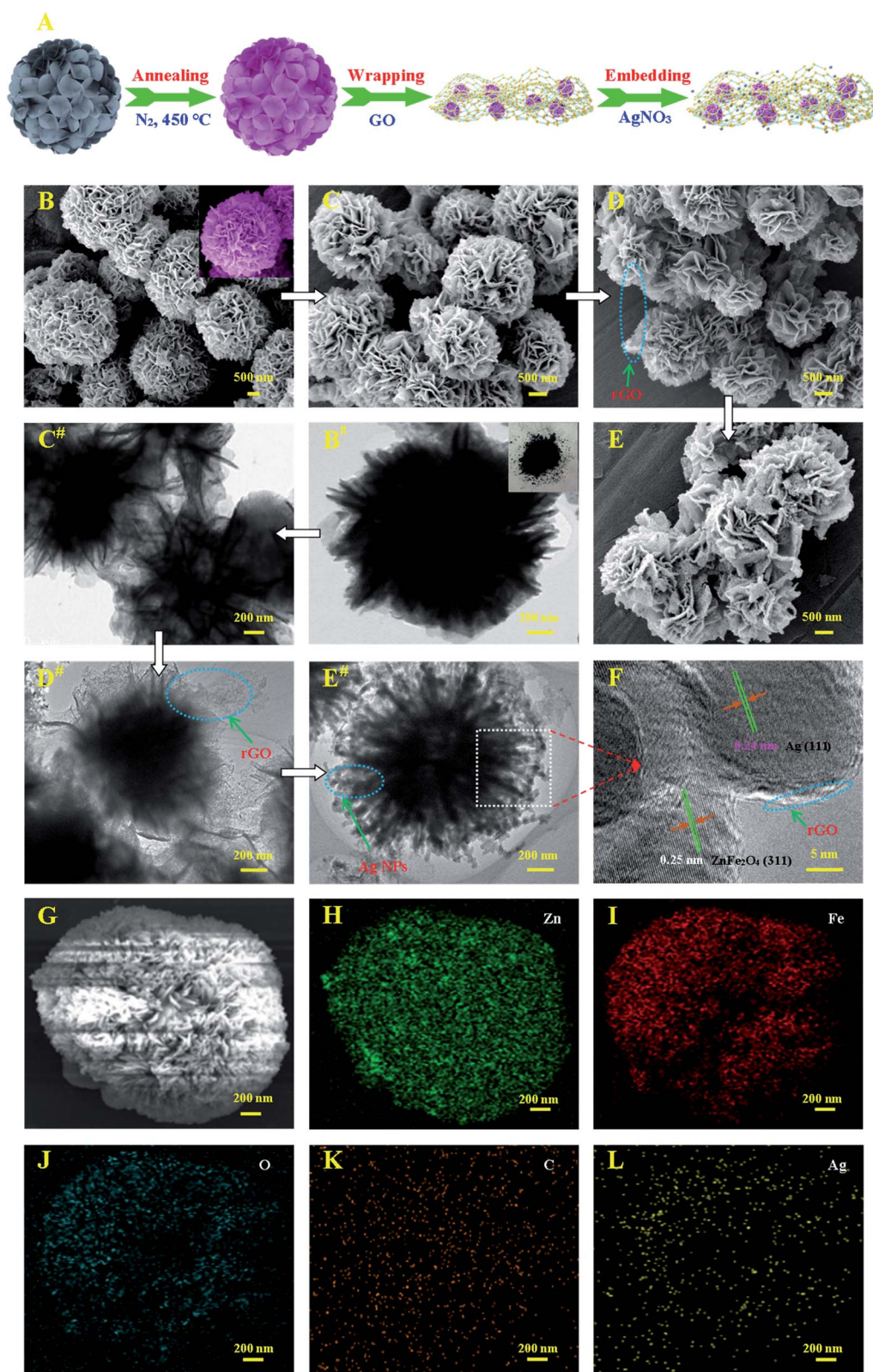


Fig. 1 (A) Schematically illustration for the formation mechanism and (B–E) FE-SEM images of as-obtained ZnFe-alkoxide precursor at various hydrothermal temperature: (B) 140 °C, (C) 160 °C, (D) 180 °C, and (E) 200 °C.







**Fig. 2** (A) Schematic illustration of the preparation process for the Ag-ZnFe<sub>2</sub>O<sub>4</sub>-rGO. The SEM images (B, C, D, and E) and TEM images (B<sup>#</sup>, C<sup>#</sup>, D<sup>#</sup>, and D<sup>#</sup>) of as-prepared ZnFe-alkoxide precursor, ZnFe<sub>2</sub>O<sub>4</sub>, ZnFe<sub>2</sub>O<sub>4</sub>-rGO, and Ag-ZnFe<sub>2</sub>O<sub>4</sub>-rGO. The insets of C and C<sup>#</sup> present the magnified FE-SEM images and as-prepared ZnFe<sub>2</sub>O<sub>4</sub>. (F) is the high-resolution image of corresponding area in E<sup>#</sup> with further enlarged images of ZnFe<sub>2</sub>O<sub>4</sub> and Ag NPs. The Energy dispersive X-ray (EDX) elemental mapping analysis of Zn (H), Fe (I), O (J), C (K) and Ag (L) elements for Ag-ZnFe<sub>2</sub>O<sub>4</sub>-rGO (G).



The specific photocatalytic degradation process is shown in Fig. S2.†

## 2.5 Reaction kinetics

Kinetic analysis was studied to evaluate the catalytic performance of Ag-ZnFe<sub>2</sub>O<sub>4</sub>-rGO more visually. It is universally acknowledged that the reaction of organic chemicals on heterogeneous catalysts can be represented by the Langmuir-Hinshelwood kinetic model. For photocatalytic degradation, ENR must first be adsorbed on the surface of the Ag-ZnFe<sub>2</sub>O<sub>4</sub>-rGO nanocomposite material and fully contacted, and then react with the reactive species on the photocatalyst for photodegradation. Put it another way, the Langmuir-Hinshelwood kinetic model can be used to depict the photocatalytic degradation of ENR by Ag-ZnFe<sub>2</sub>O<sub>4</sub>-rGO:<sup>28</sup>

$$r_0 = \frac{dC_t}{dt} = \left( k_r \frac{K_a C_t}{1 + K_a C_t} \right) \quad (2)$$

where  $r_0$  is the initial rate for ENR photodegradation reaction,  $C_t$  is the ENR concentration (mg L<sup>-1</sup>),  $k_r$  is the intrinsic rate constant,  $K_a$  is the Langmuir coefficient of ENR, and  $t$  is the reaction time (min). When the value of  $K_a C_t$  is much less than 1, eqn (2) can be simplified to the pseudo-first-order kinetics:

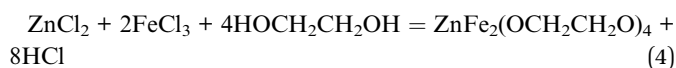
$$\ln \frac{C_t}{C_0} = -k_{pfo} t \quad (3)$$

where  $k_{pfo}$  is the pseudo-first-order reaction rate constant for ENR photodegradation (min<sup>-1</sup>).

## 3. Result and discussion

### 3.1 Structure and morphology characterization of the Ag-ZnFe<sub>2</sub>O<sub>4</sub>-rGO nanocomposites

In this study, we found that the hydrothermal temperature has an important influence on the morphology of the pre-synthesized ZnFe-alkoxide precursor, which was transferred into ZnFe<sub>2</sub>O<sub>4</sub> with conformal morphology finally after a facile thermal treatment in N<sub>2</sub>. The possible morphological evolution process to form the ZnFe-alkoxide precursor is schematically depicted in Fig. 1A. The reaction equation can be briefly depicted as follows:



Moreover, the alkaline substance (urea) added in the solution system rapidly decomposed and released a large number of NH<sub>3</sub> (alkaline) to eliminate the adverse effects of H<sup>+</sup> (HCl) generated in the reaction process (NH<sub>3</sub> + H<sup>+</sup> = NH<sub>4</sub><sup>+</sup>), thus greatly facilitating the nucleation and growth of ZnFe-alkoxide precursor.<sup>29</sup> When the reaction system was maintained at 140 °C for 12 h, only some ZnFe-alkoxide microspheres could be clearly observed (Fig. 1B) with the size of approximately 200 nm in diameter. With the reaction temperature gradually increasing to 160 °C for 12 h, the ZnFe-alkoxide nanospheres became larger, and cracks appeared on the surface to form

sheets (Fig. 1C). Increasing the temperature to 180 °C leads to the continuous growth of these sheet-like subunits, thus forming pompon mum flower-like ZnFe-alkoxide precursor (Fig. 1D). On the contrary, with the continuous increase of the hydrothermal temperature to 200 °C (Fig. 1D), the flower-like structure of ZnFe-alkoxide is severely destroyed by the high temperature and gradually evolved into monodisperse plate-like morphology with irregular edges. Obviously, the hydrothermal temperature performs an important role in controlling the morphology of the finally obtained 3D ZnFe<sub>2</sub>O<sub>4</sub> nanoflowers. That is to say, it is crucial to sustain the hydrothermal temperature at about 180 °C to obtain 3D flower-like ZnFe<sub>2</sub>O<sub>4</sub> in large-scale in this research.

The detailed morphology and structure of ZnFe<sub>2</sub>O<sub>4</sub>, ZnFe<sub>2</sub>O<sub>4</sub>-rGO, and Ag-ZnFe<sub>2</sub>O<sub>4</sub>-rGO were further characterized by SEM, TEM and HRTEM, as depicted in Fig. 2. ZnFe<sub>2</sub>O<sub>4</sub> nanoflowers were first prepared by the hydrothermal method. Fig. 2A is a schematic diagram of the synthesis process of Ag-ZnFe<sub>2</sub>O<sub>4</sub>-rGO. Typical SEM and TEM images of the ZnFe-alkoxide precursor are shown in Fig. 2B and B<sup>#</sup>. The magnified FE-SEM image of the inset in Fig. 2B depicts that the thickness of nanosheets is 10–30 nm. Compared with the ZnFe-alkoxide, the morphology of the ZnFe<sub>2</sub>O<sub>4</sub> products has obvious change after thermal treatment, and the products are composed of many uniform microspheres assembled by nanosheets (Fig. 2C and C<sup>#</sup>). Fig. 2D and D<sup>#</sup> provide representative images of the ZnFe<sub>2</sub>O<sub>4</sub>-rGO composite. It can be clearly seen that the rGO has been dispersed on the surface of the ZnFe<sub>2</sub>O<sub>4</sub> and formed a good coating on it. From Fig. 2E and E<sup>#</sup>, we can observe that the Ag-ZnFe<sub>2</sub>O<sub>4</sub>-rGO has pompon mum flower-like structure, with the size about 2–3 μm. Ag NPs were deposited on the surface of the large rGO sheets. Both the edge of rGO and the nanostructure of ZnFe<sub>2</sub>O<sub>4</sub> nanoflowers and Ag NPs could be observed clearly in the TEM image of higher magnification (Fig. 2F). This strong mutual interaction among the ZnFe<sub>2</sub>O<sub>4</sub>, Ag NPs, and the graphene sheets enables rapid electron transport, thus guaranteeing efficient chemical performance. Based on the area-selected HRTEM images (Fig. 2E<sup>#</sup> and F), the (311) plane of ZnFe<sub>2</sub>O<sub>4</sub> with a lattice spacing of 0.25 nm and phase metallic Ag (111) plane with a lattice spacing of 0.24 nm indicate them to be in an intimate interface contact, which is in favor of the charge separation.<sup>23</sup> This shows that a heterojunction was formed between ZnFe<sub>2</sub>O<sub>4</sub> and rGO, as well as Ag NPs. As shown in Fig. 2H–L, the chemical compositions of Ag-ZnFe<sub>2</sub>O<sub>4</sub>-rGO were obtained through energy dispersive X-ray spectroscopy (EDS). Zn, Fe, O, C and Ag elements were detected in the selected range (the rectangular regions marked in Fig. 2G). Obviously, C and Ag elements were uniformly distributed on the surface of ZnFe<sub>2</sub>O<sub>4</sub> without any significant aggregation (Fig. 2K and L).

The X-ray diffraction (XRD) patterns were characterized to check the phase structure of as-synthesized precursor, ZnFe<sub>2</sub>O<sub>4</sub>, Ag-ZnFe<sub>2</sub>O<sub>4</sub>, Ag-ZnFe<sub>2</sub>O<sub>4</sub>-rGO (Fig. 3). For these XRD patterns, the peaks at 30.3°, 35.8°, 43.3°, 53.9°, 57.2°, and 62.8° are indexed to the (220), (311), (400), (422), (511), and (440) crystal planes of spinel-type ZnFe<sub>2</sub>O<sub>4</sub> (JCPDS 22-1012), respectively. For the ZnFe<sub>2</sub>O<sub>4</sub>-rGO, an additional weak broad peak is observed at 17–21°, which can be indexed to reduced graphene oxide. Bare





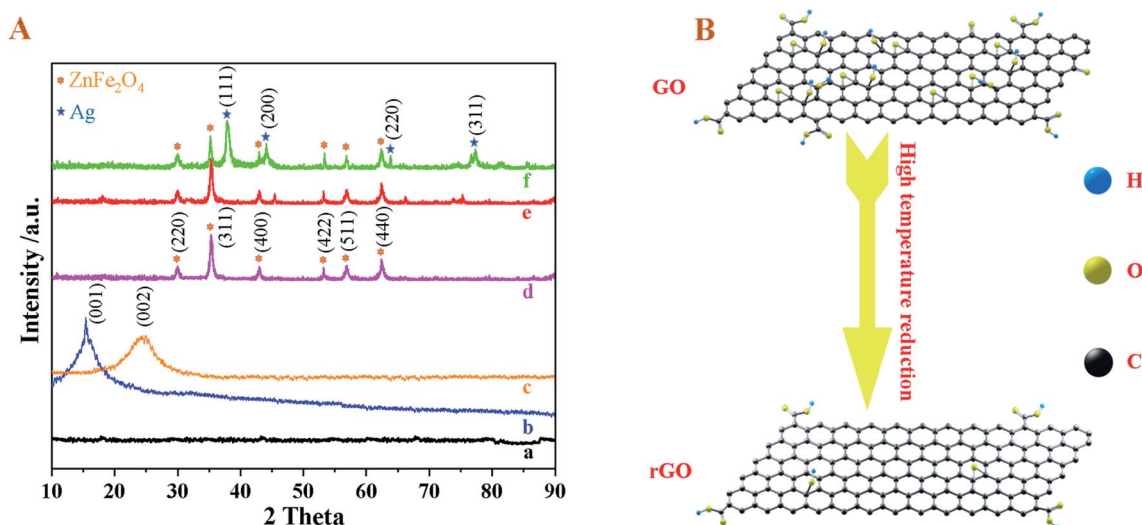


Fig. 3 (A) XRD pattern of (a) ZnFe-alkoxide precursor, (b) GO, (c) rGO, (d) bare ZnFe<sub>2</sub>O<sub>4</sub>, (e) ZnFe<sub>2</sub>O<sub>4</sub>-rGO, and (f) Ag-ZnFe<sub>2</sub>O<sub>4</sub>-rGO. (B) Schematic diagram of the reduction process of GO.

rGO exhibits its characteristic peak (002) at the 20–25°, but the XRD peak for rGO is not detected in the Ag-ZnFe<sub>2</sub>O<sub>4</sub>-rGO. This can be attributed to the effective minimization of the restacking of rGO sheets after reduction by anchoring Ag and ZnFe<sub>2</sub>O<sub>4</sub> nanoflowers as spacers.<sup>30</sup> Moreover, additional XRD peaks at 38.06°, 44.22°, 64.42°, and 77.47° is assigned to the (111), (200), (220), and (311) crystal planes of Ag NPs (JCPDS 04-0783) in the Ag-ZnFe<sub>2</sub>O<sub>4</sub>-rGO.<sup>31</sup> In addition, it is clear that the peak at 10.96° is attributed to (001) plane of GO. A broad peak at 24.60° is observed and the peak of GO is vanished in rGO, which suggests the GO was reduced mostly by heat treatment and rGO was prepared successfully. However, the diffraction peak of rGO crystal surface (002) disappears in that of the Ag-ZnFe<sub>2</sub>O<sub>4</sub>-rGO, which suggested that the ordered stacking of rGO layer was destroyed when the ZnFe<sub>2</sub>O<sub>4</sub> nanoflowers and Ag NPs were loaded synchronously on rGO surface.<sup>32</sup>

The surface electronic status and elemental composition of the Ag-ZnFe<sub>2</sub>O<sub>4</sub>-rGO nanocomposite can be seen on the X-ray photoelectron spectroscopy (XPS) in Fig. 4. The survey spectra (Fig. 4A) reveals the presence of the Zn 2p, Fe 2p, Ag 3d, O 1s, and C 1s energy regions. It can be easily found in Fig. 4B that the high-resolution Zn 2p spectrum denoted two major fitting peaks centered at 1044.8 and 1021.7 eV, which are assigned to Zn 2p<sub>1/2</sub> and Zn 2p<sub>3/2</sub>, respectively, confirming about the existence of Zn(II) oxidation state in the ZnFe<sub>2</sub>O<sub>4</sub>.<sup>33</sup> In terms of the Fe 2p spectrum (Fig. 4C), the binding energies for Fe 2p<sub>3/2</sub> at 713.1 and 711.4 eV correspond to the tetrahedral and octahedral sites, respectively. Moreover, the peak corresponding to a binding energy of 725.6 eV is in accordance with the Fe 2p<sub>1/2</sub>, and the two shake-up satellite signals (at 719.3 and 732.8 eV) also indicate that only Fe<sup>3+</sup> was present in the ZnFe<sub>2</sub>O<sub>4</sub>.<sup>34</sup> Eventually, these analyses confirm the Fe(III) oxidation state in the ZnFe<sub>2</sub>O<sub>4</sub> sample.<sup>35</sup> The distinctive peaks of Ag (Fig. 4D) at binding energies of 368.1 and 374.4 eV are well ascribed as Ag-3d<sub>5/2</sub> and Ag-3d<sub>3/2</sub>, respectively. Astonishingly, the doublet of Ag-3d has

a fissure close to 6.0 eV, indicating the presence of metallic Ag in the Ag-ZnFe<sub>2</sub>O<sub>4</sub>-rGO.<sup>4</sup> As represented in Fig. 4E, the O 1s spectrum can be divided into 3 different peaks at 530.4, 531.8 and 532.8 eV. The O 1s binding energy of 530.4 eV is assigned to the Fe-O and Zn-O. Meanwhile, the peaks with binding energies of 531.8 and 532.8 eV are assigned to the surface-absorbed oxygen species, and the presence of residual oxygen-containing groups bonded with carbon in graphene (such as C=O and C-O), respectively.<sup>36</sup> The chemisorbed oxygen on the Ag-ZnFe<sub>2</sub>O<sub>4</sub>-rGO surface is the most active oxygen, which plays a part and parcel role in the oxidation reaction.<sup>37</sup> As shown in the high resolution XPS spectra of C 1s (Fig. 4F), the peaks at 288.5, 285.3, and 284.5 eV are due to the C in C=O, C-O, and C=C/C-C. Obviously, it can be seen that the intensity of C=O and C-O are lower than C-C and C=C, which indicates that oxygen-containing groups in GO has been reduced by high temperature heat treatment.<sup>38</sup> A schematic diagram of the heat treatment process is depicted in Fig. 3B. Based on what has been mentioned above (EDS, XRD, and XPS analysis), the Ag-ZnFe<sub>2</sub>O<sub>4</sub>-rGO composites were successfully synthesized *via* a facile hydrothermal approach, followed by a photo-reduction process.

FT-IR analysis was used to confirm the functionalization of the synthesized photocatalyst. Fig. 5A and S3† reveal the FT-IR spectra of the as-obtained samples. The peaks of GO that appearing at 1051, 1230, 1420, 1614, and 1735 cm<sup>-1</sup> are assigned to C-O stretching vibration from alkoxy groups, C-O stretching vibration of epoxide, O-H stretching vibration of carbonyl, conjugate C=C skeletal stretching vibration of unoxidized graphite domains or the remaining sp<sup>2</sup> C character of graphite, and C=O stretching vibration of carbonyl and carbonyl groups, respectively. For rGO, the absence of most bands related to the above oxygen-containing functional groups demonstrates that the GO was reduced mostly by high temperature heat treatment. Further, the peak at 1590 cm<sup>-1</sup> is



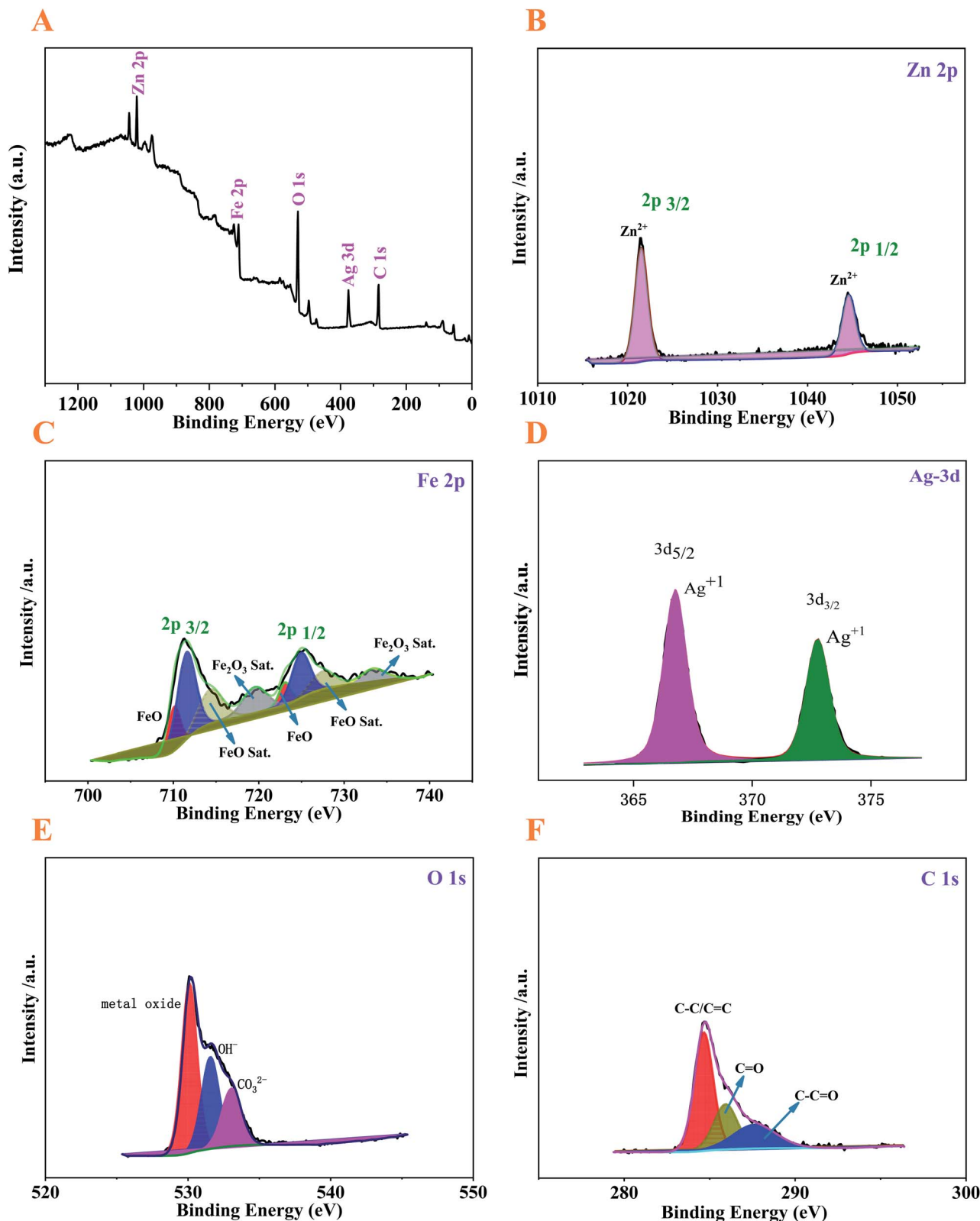


Fig. 4 XPS of the Ag-ZnFe<sub>2</sub>O<sub>4</sub>-rGO nanocomposite: (A) survey scan spectrum and sub-spectra of (B) Zn 2p, (C) Fe 2p, (D) Ag 3d, (E) O 1s, and (F) C 1s.

attributed to the conjugate C=C skeletal stretching vibration of graphite.<sup>28,33</sup> The presence of broad absorption bands at 1650 and 3410 cm<sup>-1</sup> are the contribution from the vibration of O-H

group of adsorbed organic residues and water on the surface of ZnFe<sub>2</sub>O<sub>4</sub>, respectively.<sup>39</sup> Interestingly, FT-IR spectra of ZnFe<sub>2</sub>O<sub>4</sub>-rGO exhibits one characteristic peak around 910 cm<sup>-1</sup>, which

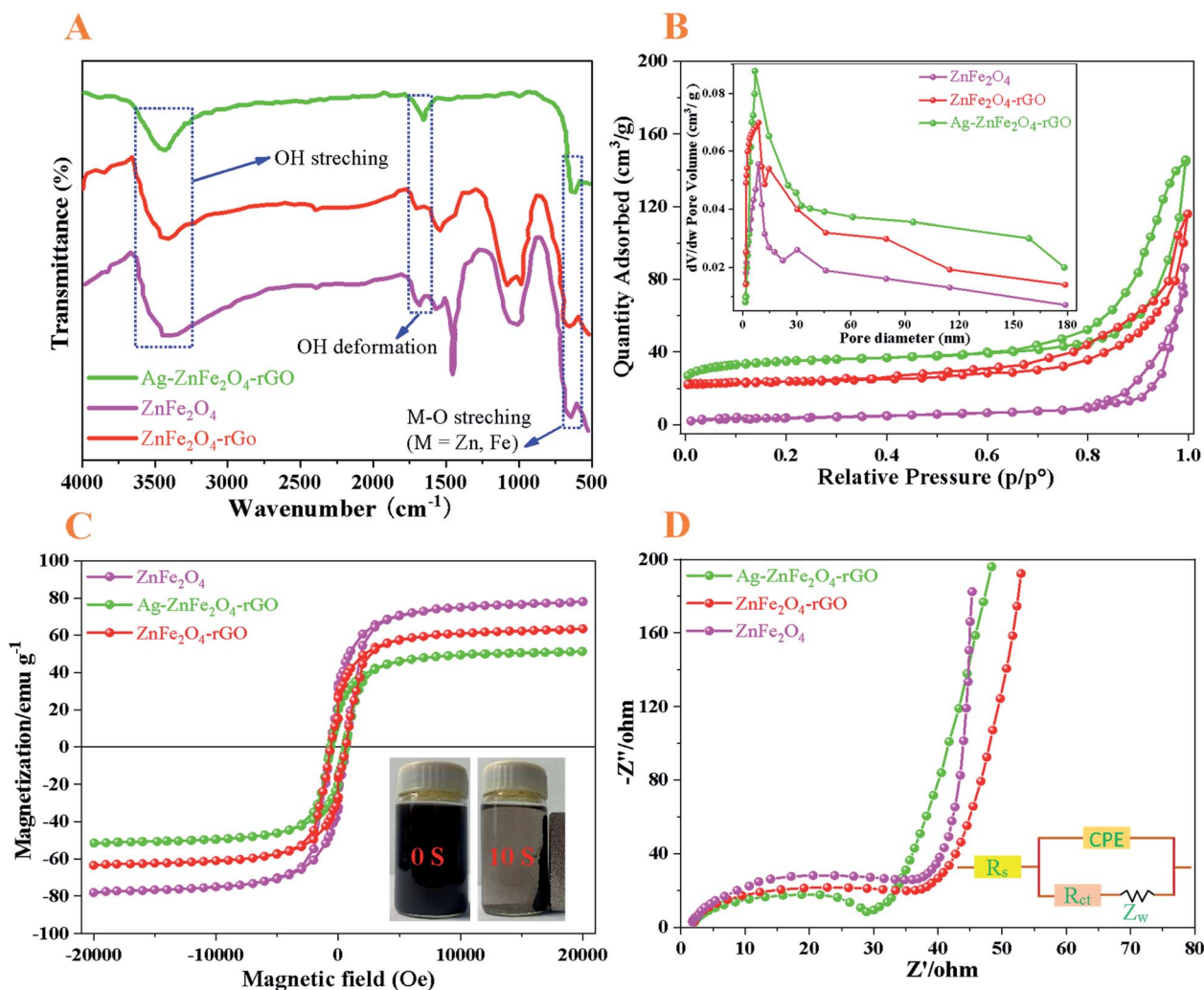


Fig. 5 (A) FT-IR spectra, (B) nitrogen adsorption–desorption isotherm, (C) M–H curves, and (D) EIS of the  $\text{ZnFe}_2\text{O}_4$ ,  $\text{ZnFe}_2\text{O}_4\text{-rGO}$ , and  $\text{Ag-ZnFe}_2\text{O}_4\text{-rGO}$ , respectively. Insert of (B) shows the pore diameter distribution of its relative samples. The inset of (C) is the magnetic separation photograph of the  $\text{Ag-ZnFe}_2\text{O}_4\text{-rGO}$ . The inset of (D) shows equivalent circuit diagram of the photo electrochemical cell.

corresponds to C–O stretching of peroxide group. In addition, the FT-IR spectrum of  $\text{Ag-ZnFe}_2\text{O}_4\text{-rGO}$  exhibits the main characteristic peaks of Fe–O and Zn–O bonds at  $590\text{--}450\text{ cm}^{-1}$  and  $\text{ZnFe}_2\text{O}_4$  at  $1650$  and  $3410\text{ cm}^{-1}$ , confirming the spinel structure of zinc ferrite.<sup>40</sup>

The porosity and specific surface area of  $\text{ZnFe}_2\text{O}_4$ ,  $\text{ZnFe}_2\text{O}_4\text{-rGO}$  and  $\text{Ag-ZnFe}_2\text{O}_4\text{-rGO}$  products were further investigated by  $\text{N}_2$  adsorption–desorption analysis, as depicted in Fig. 5B. According to the IUPAC classification, the  $\text{Ag-ZnFe}_2\text{O}_4\text{-rGO}$  exhibits the type-IV isotherm with a hysteresis loop in the relative pressure range of  $0.4\text{--}1.0$ , suggesting the existence of abundant mesopores in the catalyst sample. The Brunauer–Emmett–Teller (BET) specific surface area (SBET) of  $\text{ZnFe}_2\text{O}_4$ ,  $\text{ZnFe}_2\text{O}_4\text{-rGO}$ , and  $\text{Ag-ZnFe}_2\text{O}_4\text{-rGO}$  were calculated to be  $32.53$ ,  $78.01$ , and  $131.25\text{ m}^2\text{ g}^{-1}$ , respectively. The inset of Fig. 5B presents the corresponding Barrett–Joyner–Halenda (BJH) pore size distribution (PSD) of the  $\text{ZnFe}_2\text{O}_4$ ,  $\text{ZnFe}_2\text{O}_4\text{-rGO}$ , and  $\text{Ag-ZnFe}_2\text{O}_4\text{-rGO}$ , showing a sharp maximum at approximately  $8.66$ ,  $9.09$  and  $7.03\text{ nm}$ , respectively, further

confirming the mesoporous nature of the as-obtained nanocomposite.<sup>41</sup> During the photocatalytic reaction, more adsorption–desorption and reaction sites can be provided through the larger surface area, leading to the improvement in photocatalytic activity.

Equally importantly, the magnetic property of photocatalysts is very useful for the separation of photocatalysts from solution after reaction by external magnetic field. In Fig. 5C, it is unveiled that the  $\text{ZnFe}_2\text{O}_4$  and  $\text{ZnFe}_2\text{O}_4\text{-rGO}$  have a ferromagnetic behavior, and the saturated magnetization ( $M_s$ ) is  $78.25$  and  $62.97\text{ emu g}^{-1}$ , respectively. When combining  $\text{ZnFe}_2\text{O}_4\text{-rGO}$  and Ag NPs together, the  $\text{Ag-ZnFe}_2\text{O}_4\text{-rGO}$  still demonstrates strong ferromagnetic character with the  $M_s$  of  $50.89\text{ emu g}^{-1}$  at room temperature. By comparing the  $M_s$  values of  $\text{ZnFe}_2\text{O}_4$  and  $\text{Ag-ZnFe}_2\text{O}_4\text{-rGO}$ , assuming that the net magnetic moment of  $\text{ZnFe}_2\text{O}_4$  doesn't change ( $= 78.25\text{ emu g}^{-1}$ ) before and after coating Ag-rGO, the mass ratio of  $\text{ZnFe}_2\text{O}_4$  and Ag-rGO can be estimated to be  $2.85 : 1$ .<sup>42</sup> Besides, due to the strong ferromagnetic property, the  $\text{Ag-ZnFe}_2\text{O}_4\text{-rGO}$  photocatalyst can





easily be collected from solution within 10 s using a magnet as shown in the inset of Fig. 5C. The acceptable magnetic power of Ag-ZnFe<sub>2</sub>O<sub>4</sub>-rGO can lead to its rapid and easy separation from contaminated solutions. Fast and easy separation ability from contaminated solution is considered as an advantage of photocatalyst.<sup>43,44</sup>

### 3.2 Photocatalytic performance analysis of Ag-ZnFe<sub>2</sub>O<sub>4</sub>-rGO photocatalyst

For a better understanding of the charge separation and transport mechanisms of the Ag-ZnFe<sub>2</sub>O<sub>4</sub>-rGO, the photocatalysts were examined using electrochemical impedance spectroscopy (EIS). The order of the arc radius of these materials is roughly ZnFe<sub>2</sub>O<sub>4</sub> < ZnFe<sub>2</sub>O<sub>4</sub>-rGO < Ag-ZnFe<sub>2</sub>O<sub>4</sub>-rGO. In connection, the lesser arc radii in the impedance spectra indicates lower separation and transfer efficiency at the photocatalysts. One of the important roles of rGO is its ability to act as an electron acceptor and transfer channel to facilitate the

separation and migration of photo-generated e<sup>-</sup>.<sup>45</sup> The electrochemical impedance graphs for all photocatalysts are given in Fig. 5D, where the radius of the semicircle in the EIS plot became smaller with the introduction of rGO and Ag NPs, indicating that the Ag-ZnFe<sub>2</sub>O<sub>4</sub>-rGO discloses the least electron transfer resistance. Additionally, for Ag-ZnFe<sub>2</sub>O<sub>4</sub>-rGO samples, the transfer of e<sup>-</sup> and h<sup>+</sup> at the interface between the electrode and electrolyte is facilitated, and Ag-ZnFe<sub>2</sub>O<sub>4</sub>-rGO with the smallest arc radius illustrates the fastest separation and transfer of photo-generated e<sup>-</sup> and h<sup>+</sup>. Remarkably, both the electron-accepting and transport properties of graphene in the Ag-ZnFe<sub>2</sub>O<sub>4</sub>-rGO nanocomposite can contribute to the suppression of charge recombination. Therefore, a higher rate of photocatalysis would be achieved.

To further investigate the intrinsic reasons behind the superior photodegradation performance of the diffuse reflectance spectra (DRS) were used to measure the energy band structure. For this purpose, the results are given in Fig. 6A. The band gap ( $E_g$ ) energies of the sample were measured by

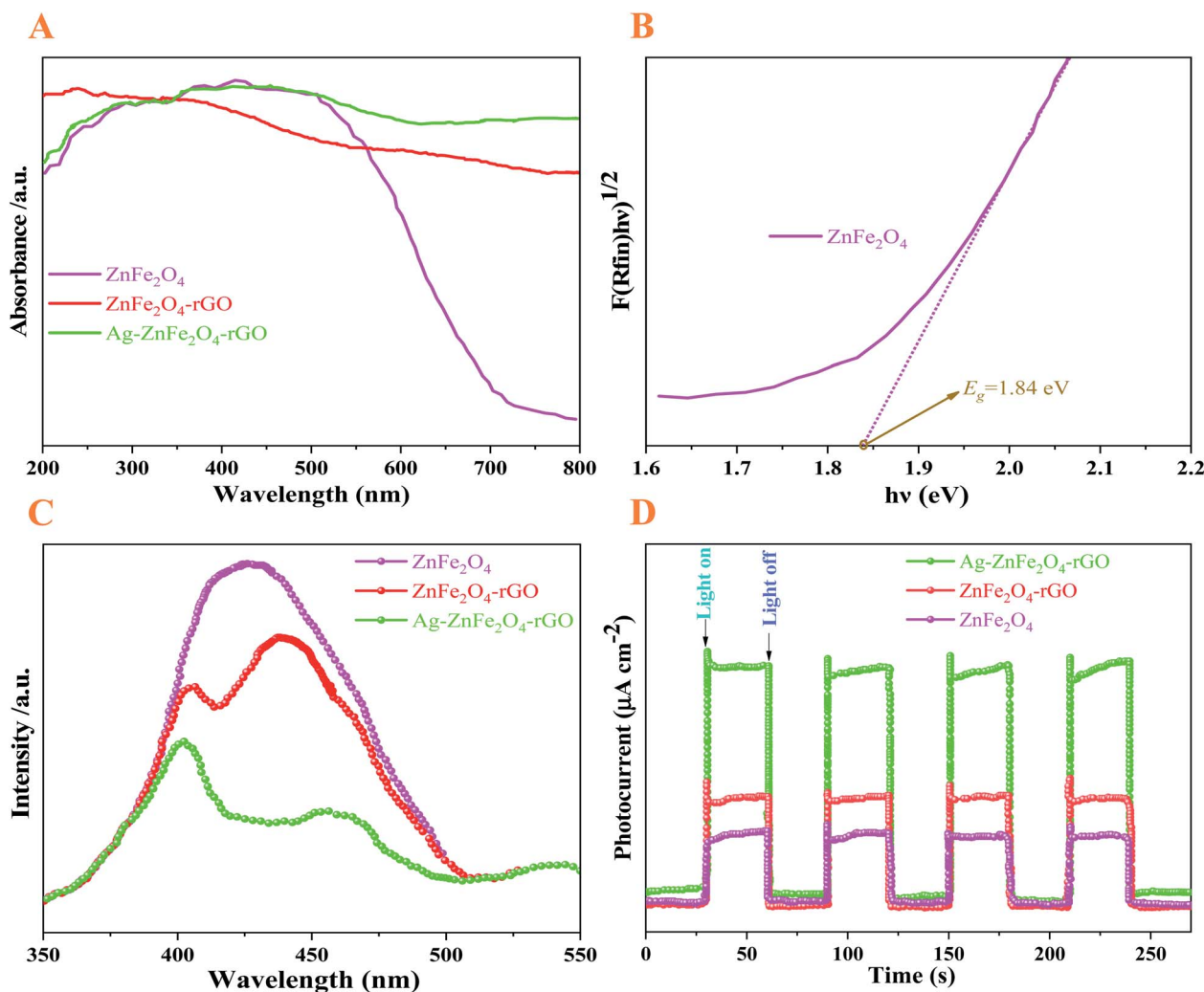


Fig. 6 The photophysical properties of the ZnFe<sub>2</sub>O<sub>4</sub>, ZnFe<sub>2</sub>O<sub>4</sub>-rGO, and Ag-ZnFe<sub>2</sub>O<sub>4</sub>-rGO materials. (A) UV-vis diffuse reflectance spectra, (B) indirect energy band gap evaluation from the plots of  $(F(R) \times hv)^{1/2}$  versus the  $hv$ , (C) room-temperature PL emission spectra, and (D) photocurrent transient response of the ZnFe<sub>2</sub>O<sub>4</sub>, ZnFe<sub>2</sub>O<sub>4</sub>-rGO, and Ag-ZnFe<sub>2</sub>O<sub>4</sub>-rGO.

transforming the diffuse reflectance spectrum into the equivalent absorption coefficient that is proportional to the Kubelka-Munk (KM) function  $F(R)$  (eqn (5)):<sup>27</sup>

$$F(R) = \frac{(1 - R)^2}{2R} = \alpha \quad (5)$$

where  $R$  is reflectance measured from an infinity thick layer of a sample ( $R = R_{\text{sample}}/R_{\text{standard}}$ ), and  $\alpha$  represents the photon energy and absorption coefficient. The band gap energies were obtained from the plots of  $(\alpha h\nu)^{1/n}$  versus the  $h\nu$  curve as the intercept of the extrapolated linear part of the plot at  $(\alpha h\nu)^{1/n} = 0$ . Herein,  $h$  = planck's constant, and  $\nu$  = the light frequency.  $n$  describes the optical transition of the photocatalyst,  $n = 0.5$  for a direct type transition (such as  $\text{ZnFe}_2\text{O}_4$ ,  $\text{C}_3\text{O}_4$ ) and  $n = 2$  for an indirect type transition ( $\text{TiO}_2$ ). Fig. 6B plots the  $(\alpha h\nu)^2$  versus the  $h\nu$  curve. The value of the band gap energy ( $E_g$ ) can be obtained by extrapolating the linear part of the curve to the horizontal axis ( $h\nu$  axis). The indirect type transition shows band gap values of 1.84 eV for  $\text{ZnFe}_2\text{O}_4$ .<sup>46</sup>

In the bare  $\text{ZnFe}_2\text{O}_4$ , Fe cations are highly sensitive to light and absorb a wide range of light extending from 200–700 nm, corresponding to a band gap of approximately 1.84 eV. The introduction of rGO increases the absorbance intensity of the composites substantially. The enhancement of visible-light absorption for the nanocomposites is caused mainly by the background absorption of rGO, as well as by the SPR effect of Ag NPs.<sup>47</sup> Extraordinarily, the intense visible-light absorption of the photocatalyst is mainly due to the metal charge transfer transitions as proposed by Hart *et al.*<sup>48</sup> It is important to know the electrons from rGO are captured by  $\text{Fe}^{3+}$  in the  $\text{ZnFe}_2\text{O}_4$  to form  $\text{Fe}^{2+}$ , the  $\text{Fe}^{2+}$  will continue react with the dissolved  $\text{O}_2$  to generate  $\text{Fe}^{3+}$ . The increase in light absorption behavior of rGO composite is attributed to the efficient separation of interlayer spacing of aromatic rings in graphene oxide and black body property.<sup>49</sup> Therefore, a greater amount of visible-light was absorbed and played an important role in the generation of more charge carriers in the photocatalyst and hence better catalytic activity. Interestingly, the results of UV-vis spectra indicated that Ag- $\text{ZnFe}_2\text{O}_4$ -rGO denoted a red shift with broad light absorbance range, which was beneficial to the higher photocatalytic performance in photocatalytic degradation reaction.<sup>50</sup>

The room-temperature photoluminescence (PL) emission spectra gave details about the recombination, migration, and shifting of photo-generated charge carriers. The higher PL intensity indicates higher recombination efficiency of photo-generated  $e^-$  and  $h^+$ . As is graphically depicted by the Fig. 6C, the PL emission intensity decreased in the following order: pure  $\text{ZnFe}_2\text{O}_4 > \text{ZnFe}_2\text{O}_4\text{-rGO} > \text{Ag-ZnFe}_2\text{O}_4\text{-rGO}$ . With introduction the rGO and Ag NPs in  $\text{ZnFe}_2\text{O}_4$  heterojunctions, the PL intensity declined, and Ag- $\text{ZnFe}_2\text{O}_4$ -rGO shows the lowest PL intensity, which unveils a direct and strong interaction between  $\text{ZnFe}_2\text{O}_4$  and carbon materials. The formed composite exhibits better charge separation compared to neat  $\text{ZnFe}_2\text{O}_4$  because the photo-excited  $e^-$  are trapped and channelized in the p skeleton of the added carbon precursor causing better separation.<sup>51</sup> It is clearly observed that  $\text{ZnFe}_2\text{O}_4$ , with being modified by rGO,

displays very low PL signal intensity, suggesting delay the recombination of  $h^+/e^-$  and more charge transfer properties. Moreover, in a restricted volume, quantum confinement of the charge carriers of  $\text{ZnFe}_2\text{O}_4$  due to size-related quantization may be responsible for the strong emission peaks. This effect may be ascribed to the electron-channelizing capacity of rGO; it traps the photo-excited electrons of  $\text{ZnFe}_2\text{O}_4$  on its  $\pi$  skeleton and reduces the recombination rate of  $h^+/e^-$ . As a result, the recombination rate of  $h^+/e^-$  pair is suppressed, and the charge separation increases in the Ag- $\text{ZnFe}_2\text{O}_4$ -rGO.<sup>52</sup> Therefore, Ag- $\text{ZnFe}_2\text{O}_4$ -rGO is likely to achieve first-rate photocatalytic activity toward the degradation of antibiotics. Further, the above claim manifest good correlation with EIS and photocatalytic result discussed in respective sections.

Under the irradiation of a 300 W Xe lamp that provided simulated solar light radiation ( $100 \text{ mW cm}^{-2}$ ), photocurrent curves were acquired by linear sweep voltammetry (LSV) scans under chopped illumination with a fixed time interval. As shown in Fig. 6D, the photocurrent responses of the hybrid nanoflowers showed cyclic alternations along with the on-off control of light. All electrodes exhibit excellent photocurrent reproducibility, suggesting that the samples were stable under the light switch cycle and the light response was reversible.<sup>51</sup> Additionally, the photocurrent density of the Ag- $\text{ZnFe}_2\text{O}_4$ -rGO samples are all significantly higher than that of  $\text{ZnFe}_2\text{O}_4$ , proving that the combination of rGO and  $\text{ZnFe}_2\text{O}_4$  nanoflowers could lead to higher optoelectronic hole pair separation efficiency. This may attribute to the electric field on the interface between  $\text{ZnFe}_2\text{O}_4$  and rGO, further confirming that the heterojunction was fabricated between  $\text{ZnFe}_2\text{O}_4$  and rGO by coating rGO on the surface of  $\text{ZnFe}_2\text{O}_4$ . It should be noted that a higher photogenerated current suggests a more efficient separation of photo-generated  $h^+/e^-$  pairs. This reveals that Ag- $\text{ZnFe}_2\text{O}_4$ -rGO stood out as the best photocatalyst among the series of samples. Consistent results were obtained in EIS studies under AM 1.5 G illumination. With all the analysis above taken into account, rGO and Ag NPs were more effective for the acceleration of interfacial charge transfer efficiency, thus improving the photocatalytic activity of the Ag- $\text{ZnFe}_2\text{O}_4$ -rGO.<sup>53</sup>

### 3.3 Photocatalytic degradation activity of Ag- $\text{ZnFe}_2\text{O}_4$ -rGO

In this study, to measure the photocatalytic degradation activities of the obtained novel multicomponent heterojunctions with 3D flower-like structures, ENR solution was first applied to model antibiotics for photocatalytic degradation under visible-light ( $\lambda = 465 \text{ nm}$ ) irradiation. It can be seen from Fig. 7, there is no obvious degradation for ENR without the presence of visible-light, indicating that light is necessary to initiate the photocatalysis. Under visible-light irradiation, using bare  $\text{ZnFe}_2\text{O}_4$  as the photocatalyst, ENR was degraded by 78.92% after 30 min, respectively. Moreover, after the introduction of rGO, the photocatalytic degradation activity significantly increased to 86.36% (ENR) and within 30 min under visible-light irradiation, respectively. Similarly, by introducing the Ag NPs to the flower-like  $\text{ZnFe}_2\text{O}_4$ -rGO, the photodegradation efficiency was enhanced to 98.68% (ENR) within 30 min under



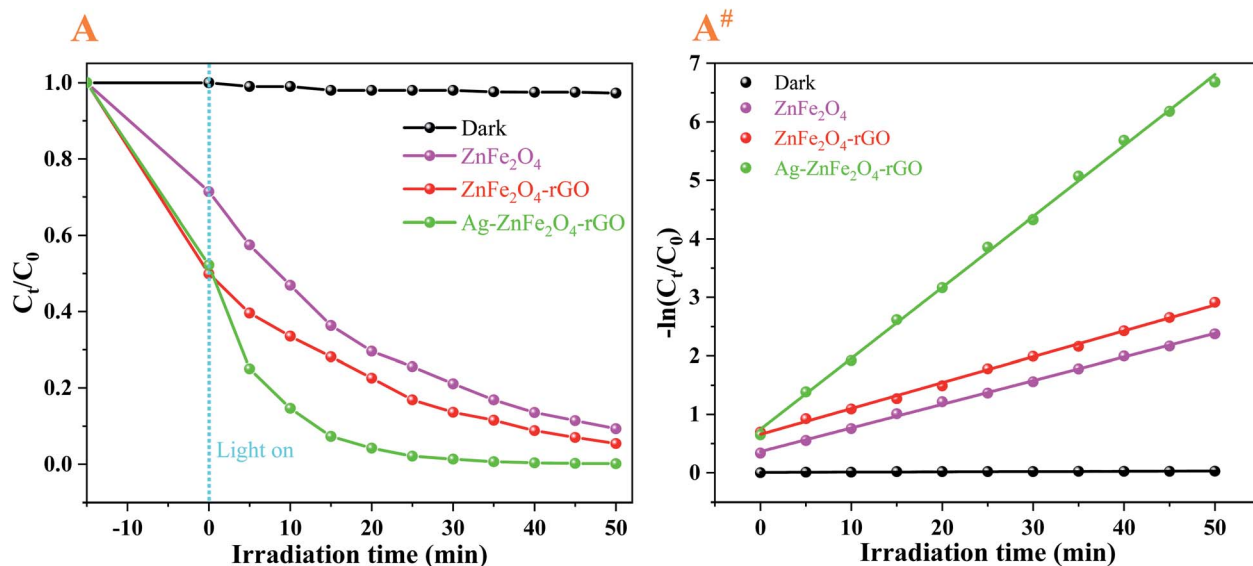


Fig. 7 Photocatalytic degradation of 10 mg·L<sup>-1</sup> ENR (A and A#) on as-prepared the ZnFe<sub>2</sub>O<sub>4</sub>, ZnFe<sub>2</sub>O<sub>4</sub>-rGO, and Ag-ZnFe<sub>2</sub>O<sub>4</sub>-rGO under visible-light ( $\lambda = 465$  nm) irradiation for comparison, respectively.

visible-light irradiation, respectively. This phenomenon is mainly caused by the SPR effect of Ag NPs. Additionally, under the stimulation of visible-light radiation, photo-generated e<sup>-</sup> can be quickly injected into the carbon layer of the rGO, and then react with the O<sub>2</sub> adsorbed on the surface of the rGO to generate 'O<sub>2</sub><sup>-</sup> radicals.<sup>21</sup> Thus, the as-prepared Ag-ZnFe<sub>2</sub>O<sub>4</sub>-rGO photocatalyst can produce more photo-generated e<sup>-</sup> and h<sup>+</sup>, as well as more superoxide anions. Due to the photo-generated e<sup>-</sup>, h<sup>+</sup> and 'O<sub>2</sub><sup>-</sup>, organic antibiotics can be oxidized and decomposed into H<sub>2</sub>O, CO<sub>2</sub> and other products.<sup>54</sup> During the electron transfer process between semiconductor materials, the charge recombination in the Ag-ZnFe<sub>2</sub>O<sub>4</sub>-rGO is inhibited, and the photocatalytic degradation efficiency is greatly improved.

### 3.4 Photocatalytic degradation reusability and stability

Fig. 8 and S4† demonstrate the photodegradation suitability of the as-obtained Ag-ZnFe<sub>2</sub>O<sub>4</sub>-rGO photocatalyst for antibiotics ENR under visible-light irradiation. The relationship between the concentration of ENR and the photodegradation time and the number of cycles illustrate that the degradation of ENR was faster when Ag-ZnFe<sub>2</sub>O<sub>4</sub>-rGO photocatalyst were used. Simultaneously, ENR could be degraded completely within 35 min under visible-light, respectively. Beyond any dispute, the stability and recyclability of photocatalysts are important parameters for their industrial and large-scale application. For this purpose, photocatalysts were collected after each degradation process and washed with 20 mL ethanol solution for 2 h then dried in an oven at 60 °C overnight, and used for the next run (Fig. S5†). After 10 repeated cycles of usage, the photodegradation efficiencies of Ag-ZnFe<sub>2</sub>O<sub>4</sub>-rGO to ENR remained at 37.64% within 50 min, respectively. It can be seen that the composite material synthesized in this study has a very superior reusability. In order to prove the photostability of Ag-ZnFe<sub>2</sub>O<sub>4</sub>-

rGO, a reusability experiment was carried out. It has been clear that after 10 cycles of degradation, a small decrease in XRD peak intensity was observed (Fig. S6†), which results in a slight reduction in photocatalytic activity. Additionally, in order to further confirm the photocatalyst morphological structure change during photocatalytic degradation process, the Ag-ZnFe<sub>2</sub>O<sub>4</sub>-rGO was imaged by the SEM after each degradation. The details are as Fig. 9. It can be clearly found that the photocatalyst after 8 cycles, the sample morphology has hardly

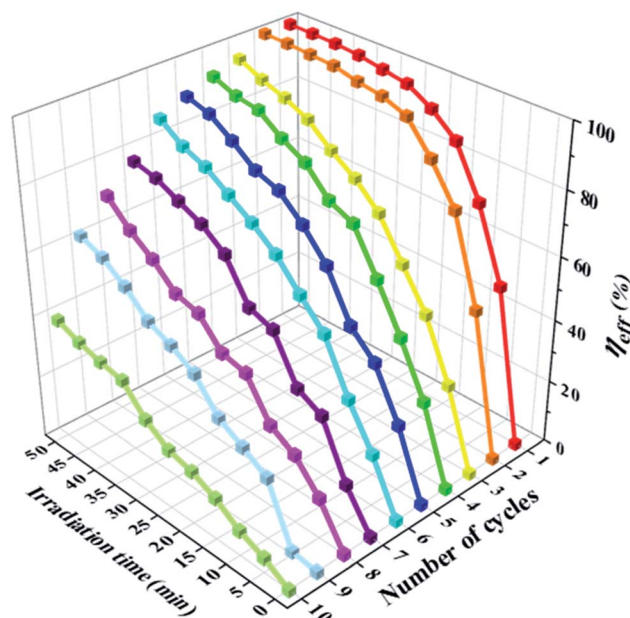


Fig. 8 Photodegradation rates curves for ENR (10 mg·L<sup>-1</sup>) aqueous solution using Ag-ZnFe<sub>2</sub>O<sub>4</sub>-rGO photocatalysts for 10 cycles under visible-light irradiation.





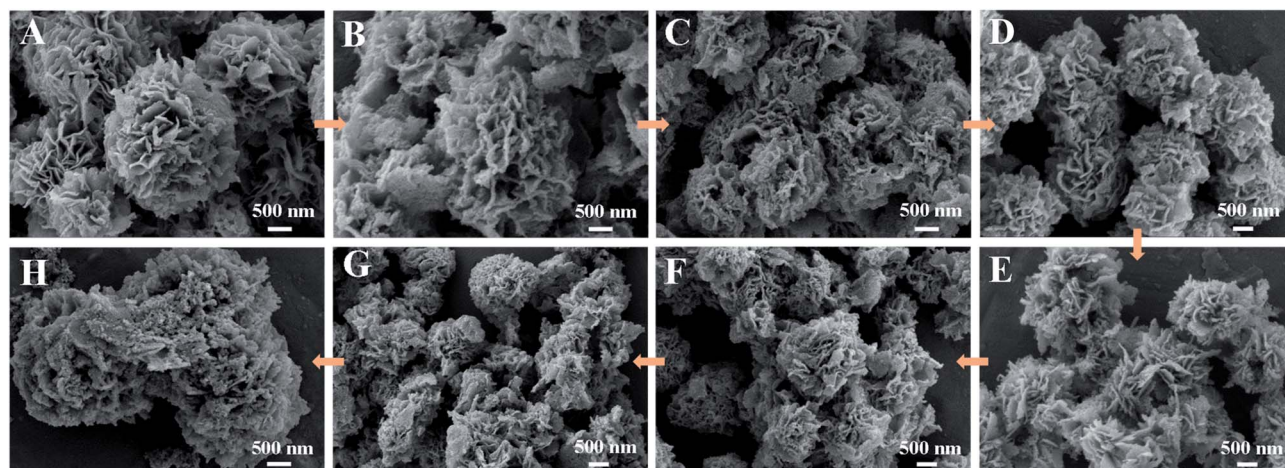


Fig. 9 (A), (B), (C), (D), (E), (F), (G), and (H) are SEM images after cyclic degradation of 1, 2, 3, 4, 5, 6, 7, and 8 times by the Ag-ZnFe<sub>2</sub>O<sub>4</sub>-rGO, successively.

significant change. Nevertheless, after 8 cycles, the morphology and structure of the Ag-ZnFe<sub>2</sub>O<sub>4</sub>-rGO sample changed significantly, almost no longer maintaining the original 3D flower-like structure. In general, the structure of the as-obtained Ag-ZnFe<sub>2</sub>O<sub>4</sub>-rGO is relatively stable. Most importantly, several studies have depicted that the photocatalytic degradation is a surface-mediated reaction and the photocatalytic efficiency and rate is highly dependent on the active sites onto the photocatalyst.<sup>55</sup> The 3D flower-like Ag-ZnFe<sub>2</sub>O<sub>4</sub>-rGO photocatalyst synthesized in this study has a larger surface area and dense reaction sites, and therefore the photocatalytic degradation performance is greatly improved. Some recently published contributions related to this are given in Table S1.† To take it a step further, according to the eqn (3), the photodegradation reaction rate constant ( $k_{\text{pfo}}$ ) can be calculated to be  $0.1212 \text{ min}^{-1}$  for ENR under visible-light.

### 3.5 Proposed photocatalytic mechanism of the Ag-ZnFe<sub>2</sub>O<sub>4</sub>-rGO

To further confirm the main active species, electron spin resonance (ESR) technology with 5,5-dimethyl-1-pyrroline *N*-oxide (DMPO) to detect the generation of  $\cdot\text{O}_2^-$  and  $\cdot\text{OH}$ . The ESR-DMPO experiments were carried out in the dark and under irradiation for 10 or 15 min. In the dark conditions, no obvious signals for both  $\cdot\text{O}_2^-$  and  $\cdot\text{OH}$  could be detected in Fig. S7.† In Fig. S7B†, the DMPO- $\cdot\text{O}_2^-$  peaks were observed under visible-light irradiation, indicating that  $\cdot\text{O}_2^-$  are produced. Furthermore, the characteristic peaks of DMPO- $\cdot\text{OH}$  and DMPO- $\cdot\text{O}_2^-$  were detected and the signal strength increased with the increase of irradiation time. The ESR experiment was carried out under different solutions, indicating that  $\cdot\text{OH}$  was formed by the  $\cdot\text{O}_2^-$  and  $\cdot\text{HO}_2$  but not directly oxidized ENR in the degradation process.<sup>34</sup> Correspondingly, the conduction band

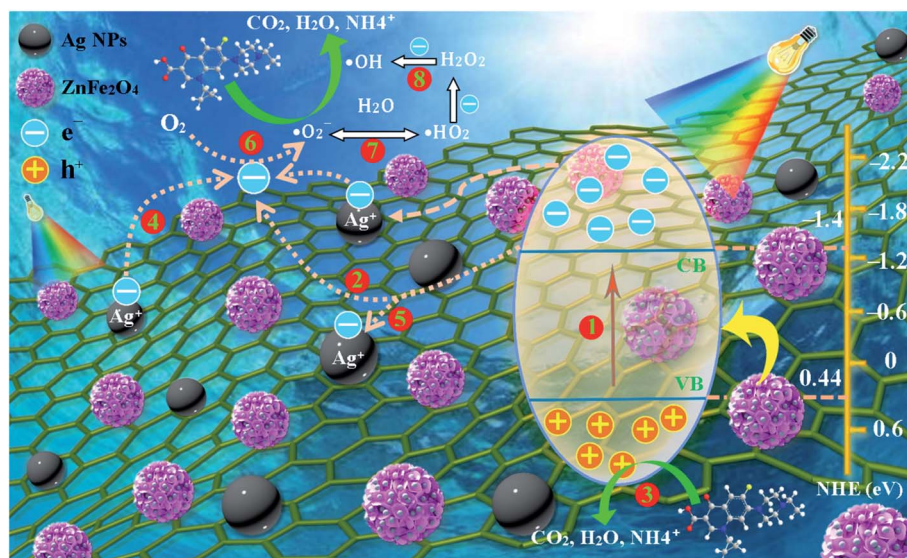


Fig. 10 Schematic diagram of the possible photocatalytic mechanism of Ag-ZnFe<sub>2</sub>O<sub>4</sub>-rGO composite under visible-light irradiation.



(CB) potential ( $E_{CB}$ ) and valence band (VB) potential ( $E_{VB}$ ) can also be calculated by the following formulas:<sup>56,57</sup>

$$E_{VB} = X - E_c + 0.5E_g \quad (6)$$

$$E_{CB} = E_{VB} - E_g \quad (7)$$

where  $X$  is the absolute electronegativity of the semiconductor, that is, the geometric mean of the absolute electronegativity of the atoms in the semiconductor ( $X_{Zn} = 4.45$  eV,  $X_{Fe} = 4.06$  eV,  $X_O = 7.54$  eV). After calculation,  $X_{ZnFe_2O_4} = 5.86$  eV.  $E_c$  and  $E_g$  are the energy of free electrons on the hydrogen scale (4.5 eV) and the band gap values of the semiconductor, respectively. Therefore, the  $E_{VB}$  and  $E_{CB}$  of the  $ZnFe_2O_4$  were estimated to be approximately +0.44 and -1.4 eV.

With the analysis above taken into account, the reasonable reaction mechanism for improving the photocatalytic activity can be offered by Fig. 10. First, through the  $e^-$  channelization ability of the rGO, the photo-excited  $e^-$  of  $ZnFe_2O_4$  are trapped on its  $\pi$  framework, and the recombination rate of photo-excited  $h^+/e^-$  is prevented, forming a stable heterojunction between Ag and  $ZnFe_2O_4$ , as well as rGO. It is generally known that the CB ( $E_{CB} = -1.4$  eV) and VB ( $E_{VB} = +0.44$  eV) of the  $ZnFe_2O_4$ . Upon visible-light irradiation,  $e^-$  in the VB of  $ZnFe_2O_4$  can be photo-excited to its CB to produce the  $h^+/e^-$  pairs after the irradiation of visible-light (pathway 1). Owing to the fact that the CB of the rGO (-0.75 eV) is more positive than that of the  $ZnFe_2O_4$  (-1.44 eV) (pathway 2), the partial photo-generated  $e^-$  from CB of  $ZnFe_2O_4$  are transferred to the surface of the rGO layers. Oppositely, the photo-generated  $h^+$  left the VB of  $ZnFe_2O_4$ , which can prohibit the recombination of  $h^+/e^-$  pair. Thus, the photo-generated  $e^-$  and  $h^+$  can be effectively separated. Meanwhile, the rGO also plays an important role in ternary composite. First of all, the unique structure of rGO provides the Ag- $ZnFe_2O_4$ -rGO with a larger surface area which can make photocatalyst absorb more light radiation and ENR. Moreover, there are a lot of defects and few excited groups containing oxygen in the rGO surface because of the reduction of GO, which can bring strong absorption capacity for the Ag- $ZnFe_2O_4$ -rGO. Finally, the conjugated p-system of rGO can also hinder the recombination of  $h^+/e^-$  pairs. Therefore, the coupling of  $ZnFe_2O_4$  and rGO can effectively reduce the recombination rate of  $e^-$  and  $h^+$ , and subsequently decreases the internal resistance as well as enhances the interfacial charge transfer efficiency, which can be seen in the EIS spectra (Fig. 5D).<sup>58</sup> Furthermore, the reactive  $h^+$  at the VB of  $ZnFe_2O_4$  will

oxidize ENR directly, because the potential of the VB of  $ZnFe_2O_4$  (0.44 eV) is more negative than the potential required to oxidize the adsorbed  $H_2O$  on the surface to  $\cdot OH$  ( $E^0(\cdot OH/H_2O) = 2.87$  eV) (pathway 3).<sup>33</sup> Meanwhile, Ag NPs can absorb light and generate electrons due to the SPR effect (Fig. 11), plasmon-induced electrons on the Ag NPs can flow to the CB of rGO rather than  $ZnFe_2O_4$  (pathways 4), owing to the less negative CB bottom of graphene compared to that of  $ZnFe_2O_4$ , and Ag NPs can also accept electrons from the CB of the  $ZnFe_2O_4$  for enhancing the charge separation. A portion of the CB electrons on  $ZnFe_2O_4$  tends to shift to the positive-potential  $Ag^+$  and changes some  $Ag^+$  to  $Ag^0$  (pathways 5), whereas the other electrons can be scavenged by  $O_2$  in the water, resulting in superoxide anion free radicals ( $\cdot O_2^-$ ) and peroxy ( $\cdot HO_2$ ) radicals [ $E^0(O_2/\cdot O_2^-) = 0.33$  V, and  $E^0(O_2/\cdot HO_2) = 0.05$  V] (pathways 6 and 7), which are the main active species in the reaction with ENR.<sup>59</sup> Since the produced  $\cdot O_2^-$  can be prolonging to more than 15 min (Fig. S7B†), the photocatalytic degradation efficiency and rate of ENR can be significantly enhanced under visible-light irradiation. In addition, the produced oxygen-containing radicals ( $\cdot O_2^-$  and  $\cdot HO_2$ ) can further react with electrons and protons to produce hydroxyl radicals ( $\cdot OH$ ) (pathway 8).<sup>60</sup> However, in this study,  $\cdot OH$  is not the main active species for photocatalytic degradation of ENR. Consequently, the separation efficiency of the photo-generated charge carriers is effectively improved at the interface of the nanocomposite, which allows more participation of  $h^+$  in the photocatalytic reaction. Thus, the Ag- $ZnFe_2O_4$ -rGO photocatalyst has high photocatalytic activity. The reaction equations can be briefly depicted as follows:

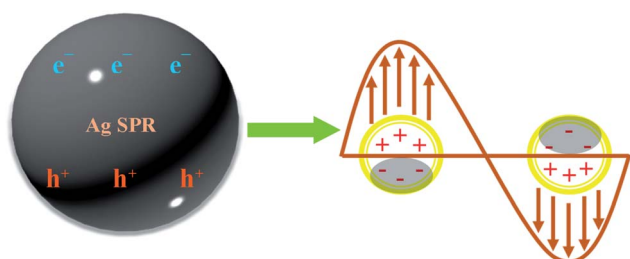
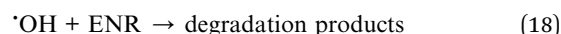
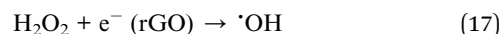
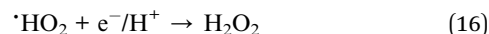
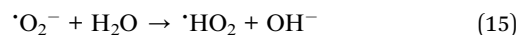
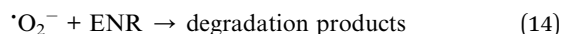
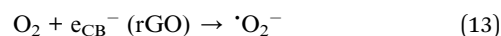
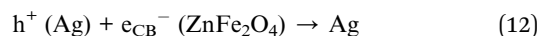
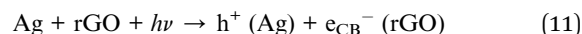
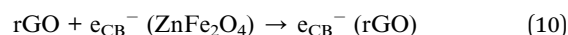
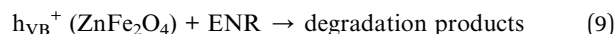
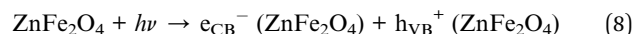


Fig. 11 Schematic diagram of the surface plasmon resonance (SPR) effect of Ag NPs.

### 3.6 Identified products on degradation of ENR

In order to explore the conversion pathway of ENR in the photocatalytic degradation process, the structures of eleven main photoproducts P1–P11 were identified by HPLC-Q-TOF-MS. For





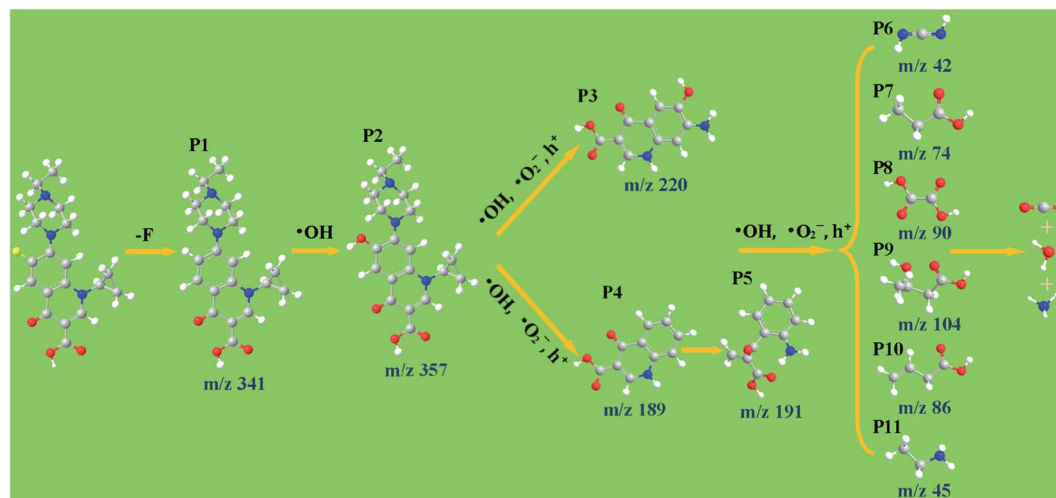


Fig. 12 Potential photocatalytic degradation pathways of ENR in the Ag–ZnFe<sub>2</sub>O<sub>4</sub>–rGO aqueous solution under visible-light irradiation.

the ENR, 11 organic intermediates were identified with the molecular weights and characteristic fragment ions shown in Table S2.† According to the experimental detection of the photodegradation intermediate and the theoretical calculation of the Fukui function, the degradation pathway of ENR in the Ag–ZnFe<sub>2</sub>O<sub>4</sub>–Ag photocatalytic process was proposed (Fig. 12). The details are as follows. First of all, the C–F bond of ENR was broken under the irradiation of UV-light (P1 ( $m/z = 341$ )), introducing the replaced –OH undergoing the attack of  $\cdot\text{OH}$ , and a typical product (P2 ( $m/z = 357$ )) for the fluoroquinolone oxidation was generated.<sup>61</sup> For the product P2, on the one hand, N20 and C11 (Fig. S8†) were attacked by  $\cdot\text{OH}$ ,  $\cdot\text{O}_2^-$  and  $h^+$ , leading to the formation of the P3 ( $m/z = 220$ ). On the other hand, the cyclopropane and piperazine groups in the P2 detach to produce P4 ( $m/z = 189$ ). Then, C8 in the intermediate P4 was further attacked by  $\cdot\text{OH}$ ,  $\cdot\text{O}_2^-$  and  $h^+$  to form product P5 ( $m/z = 191$ ). As a result, under the continuous attack of the reactive species, the quinolone ring and the benzene ring are destroyed and cleaved through a ring-opening reaction, and then *via* oxidation reactions to obtain smaller organic products (P7–P11). Finally, the intermediate products could be completely mineralized to CO<sub>2</sub>, H<sub>2</sub>O and NH<sub>4</sub><sup>+</sup>.

## 4. Conclusions

To conclude, Ag–ZnFe<sub>2</sub>O<sub>4</sub>–rGO photocatalysts were synthesized *via* a facile hydrothermal approach and heat treatment, followed by a photo-reduction process. The oxidation resistance of rGO could effectively maintain the structural and chemical stability of Ag–ZnFe<sub>2</sub>O<sub>4</sub>. Through the electron channelization ability of rGO, the photo-excited  $e^-$  of ZnFe<sub>2</sub>O<sub>4</sub> were trapped on its  $\pi$  framework, and the recombination rate of  $e^-/h^+$  was prevented, forming a stable heterojunction between Ag–ZnFe<sub>2</sub>O<sub>4</sub> and rGO. The photocatalytic activity of Ag–ZnFe<sub>2</sub>O<sub>4</sub>–rGO was improved under visible-light. ENR were degraded completely within 35 min under visible-light illumination. Moreover, the photodegradation reaction rate constant ( $k_{\text{prf}}$ ) could be

calculated to be 0.1212 min<sup>−1</sup> for ENR. Heterojunctions between Ag and ZnFe<sub>2</sub>O<sub>4</sub>–rGO can effectively separate photo-generated carriers, and the high surface area of 3D flower-like ZnFe<sub>2</sub>O<sub>4</sub> provides more reactive sites. The excellent conductivity of rGO facilitates rapid transfer of photoelectrons. Additionally, the *in situ* generated H<sub>2</sub>O<sub>2</sub>,  $h^+$  and  $\cdot\text{O}_2^-$  can degrade organic antibiotics through effective oxidation and mineralization. This research provides new ideas for the design and manufacture of heterojunction photocatalysts, as well as new ideas for environmental protection and sustainable development.

## Conflicts of interest

There are no conflicts to declare.

## Acknowledgements

This work was supported by financial support from Dr Wang Juan from Shaanxi Normal University and Shaanxi Institute of International Trade & Commerce, and guidance from Zhang Chun (Associate Professor) and Jin Xiaodong from Lanzhou Jiaotong University. The author would like to thank the TEM images tested by the Shanghai Spectrochemical Technical Service Center, China. Professor Yang Guohua from Lanzhou Jiaotong University is thanked for her English revision.

## References

- 1 J. Huang, D. Li, R. Li, Q. Zhang, T. Chen, H. Liu, Y. Liu, W. Lv and G. Liu, An efficient metal-free phosphorus and oxygen co-doped g-C<sub>3</sub>N<sub>4</sub> photocatalyst with enhanced visible light photocatalytic activity for the degradation of fluoroquinolone antibiotics, *Chem. Eng. J.*, 2019, 374, 242–253.
- 2 F. Guo, J. Chen, J. Zhao, Z. Chen, D. Xia, Z. Zhan and Q. Wang, Z-scheme heterojunction g-C<sub>3</sub>N<sub>4</sub>@PDA/BiOBr





- with biomimetic polydopamine as electron transfer mediators for enhanced visible-light driven degradation of sulfamethoxazole, *Chem. Eng. J.*, 2020, **386**, 124014.
- 3 X. Wen, C. Niu, L. Zhang, C. Liang and G. Zeng, A novel Ag<sub>2</sub>O/CeO<sub>2</sub> heterojunction photocatalysts for photocatalytic degradation of enrofloxacin: possible degradation pathways, mineralization activity and an in depth mechanism insight, *Appl. Catal., B*, 2018, **221**, 701–714.
  - 4 D. Qiao, Z. Li, J. Duan and X. He, Adsorption and photocatalytic degradation mechanism of magnetic graphene oxide/ZnO nanocomposites for tetracycline contaminants, *Chem. Eng. J.*, 2020, **400**, 125952.
  - 5 Y. Wang, C. Zhu, G. Zuo, Y. Guo, W. Xiao, Y. Dai, J. Kong, X. Xu, Y. Zhou, A. Xie, C. Sun and Q. Xian, 0D/2D Co<sub>3</sub>O<sub>4</sub>/TiO<sub>2</sub> Z-Scheme heterojunction for boosted photocatalytic degradation and mechanism investigation, *Appl. Catal., B*, 2020, **278**, 119298.
  - 6 P. Veerakumar, A. Sangili, S. Manavalan, P. Thanasekaran and K. Lin, Research Progress on Porous Carbon Supported Metal/Metal Oxide Nanomaterials for Supercapacitor Electrode Applications, *Ind. Eng. Chem. Res.*, 2020, **59**, 6347–6374.
  - 7 Y. Li, Y. Lia, Y. Yin, D. Xia, H. Ding, C. Ding, J. Wu, Y. Yan, Y. Liu, N. Chen, P. Wong and A. Lu, Facile synthesis of highly efficient ZnO/ZnFe<sub>2</sub>O<sub>4</sub> photocatalyst using earth abundant sphalerite and its visible light photocatalytic activity, *Appl. Catal., B*, 2018, **226**, 324–336.
  - 8 K. Li, Y. Luo, L. Gao, T. Li and G. Duan, Au-Decorated ZnFe<sub>2</sub>O<sub>4</sub> Yolk–Shell Spheres for Trace Sensing of Chlorobenzene, *ACS Appl. Mater. Interfaces*, 2020, **12**, 16792–16804.
  - 9 H. Song, L. Zhu, Y. Li, Z. Lou, M. Xiao and Z. Ye, Preparation of ZnFe<sub>2</sub>O<sub>4</sub> nanostructures and highly efficient visible-light-driven hydrogen generation with the assistance of nanoheterostructures, *J. Mater. Chem. A*, 2015, **3**, 8353–8360.
  - 10 P. Koley, S. Shit, B. Joseph, S. Pollastri, Y. Sabri, E. Mayes, L. Nakka, J. Tardio and J. Mondal, Leveraging Cu/CuFe<sub>2</sub>O<sub>4</sub>-Catalyzed Biomass-Derived Furfural Hydrodeoxygenation: A Nanoscale Metal–Organic–Framework Template Is the Prime Key, *ACS Appl. Mater. Interfaces*, 2020, **12**, 21682–21700.
  - 11 I. Gerber and P. Serp, A Theory/Experience Description of Support Effects in Carbon Supported Catalysts, *Chem. Rev.*, 2020, **120**, 1250–1349.
  - 12 P. Lin, G. He, J. Chen, A. Dwivedi and S. Hsieh, Monitoring the photoinduced surface catalytic coupling reaction and environmental exhaust fumes with an Ag/PDA/CuO modified 3D glass microfiber platform, *J. Ind. Eng. Chem.*, 2020, **82**, 424–432.
  - 13 Y. Ge, J. Liu, X. Liu, J. Hu, X. Duan and X. Duan, Rapid Electrochemical Cleaning Silver Nanowire Thin Films for High-Performance Transparent Conductors, *J. Am. Chem. Soc.*, 2019, **141**, 12251–12257.
  - 14 D. Chen, Z. Lin, M. Sartin, T. Huang, J. Liu, Q. Zhang, L. Han, J. Li, Z. Tian and D. Zhan, Photosynergetic Electrochemical Synthesis of Graphene Oxide, *J. Am. Chem. Soc.*, 2020, **142**, 6516–6520.
  - 15 A. Mohammed, S. Usgaonkar, F. Kanheerampockil, S. Karak, A. Halder, M. Tharkar, M. Addicoat, T. Ajithkumar and R. Banerjee, Connecting Microscopic Structures, Mesoscale Assemblies, and Macroscopic Architectures in 3D-Printed Hierarchical Porous Covalent Organic Framework Foams, *J. Am. Chem. Soc.*, 2020, **142**, 8252–8261.
  - 16 M. Yang, N. Zhang and Y. Xu, Synthesis of fullerene-, carbon nanotube-, and graphene–TiO<sub>2</sub> nanocomposite photocatalysts for selective oxidation: a comparative study, *ACS Appl. Mater. Interfaces*, 2013, **22**, 1156–1164.
  - 17 Z. Yao, M. Hu, Z. Iqbal and X. Wang, N<sup>8–</sup> Polynitrogen Stabilized on Boron-Doped Graphene as Metal-Free Electrocatalysts for Oxygen Reduction Reaction, *ACS Catal.*, 2020, **10**, 160–167.
  - 18 N. Khadgi, Y. Li, A. Upreti, C. Zhang, W. Zhang, Y. Wang and D. Wang, Enhanced Photocatalytic Degradation of 17 $\alpha$ -Ethinylestradiol Exhibited by Multifunctional ZnFe<sub>2</sub>O<sub>4</sub>-Ag/rGO Nanocomposite Under Visible Light, *Photochem. Photobiol.*, 2016, **92**, 238–246.
  - 19 N. Han, W. Wang, X. Lv, W. Zhang, C. Yang, M. Wang, X. Kou, W. Li, Y. Dai and X. Zhang, Highly Efficient Purification of Multicomponent Wastewater by Electrospinning Kidney–Bean–Skin-like Porous H-PPAN/rGO-g-PAO@Ag<sup>+</sup>/Ag Composite Nanofibrous Membranes, *ACS Appl. Mater. Interfaces*, 2019, **11**, 46920–46929.
  - 20 M. Zhang, F. Zhao, T. An, Y. Yang, H. Li, Q. Pan, X. Wang and Z. Jiang, Catalytic Effects of rGO-MFe<sub>2</sub>O<sub>4</sub> (M = Ni, Co, and Zn) Nanocomposites on the Thermal Decomposition Performance and Mechanism of Energetic FOX-7, *J. Phys. Chem. A*, 2020, **124**, 1673–1681.
  - 21 A. Mady, M. Baynosa, D. Tuma and J. Shim, Facile microwave-assisted green synthesis of Ag–ZnFe<sub>2</sub>O<sub>4</sub>@rGO nanocomposites for efficient removal of organic antibiotics under UV- and visible-light irradiation, *Appl. Catal., B*, 2017, **203**, 416–427.
  - 22 S. Liu, X. Zhu, Y. Zhou, Z. Meng, Z. Chen, C. Liu, F. Chen, Z. Wu and J. Qian, Ultrahigh cycling stability and rate capability of ZnFe<sub>2</sub>O<sub>4</sub>@graphene hybrid anode prepared through a facile syn-graphenization strategy, *Catal. Sci. Technol.*, 2017, **7**, 3210–3219.
  - 23 J. Li, F. Wei, C. Dong, W. Mu and X. Han, A Z-scheme ZnFe<sub>2</sub>O<sub>4</sub>/RGO/In<sub>2</sub>O<sub>3</sub> hierarchical photocatalyst for efficient CO<sub>2</sub> reduction enhancement, *J. Mater. Chem. A*, 2020, **8**, 6524–6531.
  - 24 H. Guo, N. Jiang, H. Wang, N. Lu, K. Shang, J. Li and Y. Wu, Pulsed discharge plasma assisted with graphene–WO<sub>3</sub> nanocomposites for synergistic degradation of antibiotic enrofloxacin in water, *Chem. Eng. J.*, 2019, **372**, 226–240.
  - 25 J. Fang, C. Zhou, Y. Chen, L. Fang, W. Wang, C. Zhu, Y. Ni and C. Lu, Efficient Photocatalysis of Composite Films Based on Plasmon Enhanced Triplet–Triplet Annihilation, *ACS Appl. Mater. Interfaces*, 2020, **12**, 717–726.
  - 26 M. Su, C. He, V. Sharma, M. Asi, D. Xia, X. Li, H. Deng and Y. Xiong, Mesoporous zinc ferrite: Synthesis, characterization, and photocatalytic activity with H<sub>2</sub>O<sub>2</sub>/visible light, *J. Hazard. Mater.*, 2012, **211**, 95–103.



- 27 Q. Zhu, Y. Sun, F. Na, J. Wei, S. Xu, Y. Li and F. Guo, Fabrication of CdS/titanium-oxo-cluster nanocomposites based on a  $\text{Ti}_{32}$  framework with enhanced photocatalytic activity for tetracycline hydrochloride degradation under visible light, *Appl. Catal., B*, 2019, **254**, 541–550.
- 28 S. Song, Y. Wang, H. Shen, J. Zhang, H. Mo, J. Xie, N. Zhou and J. Shen, Ultrasmall Graphene Oxide Modified with  $\text{Fe}_3\text{O}_4$  Nanoparticles as a Fenton-Like Agent for Methylene Blue Degradation, *ACS Appl. Nano Mater.*, 2019, **2**, 7074–7084.
- 29 L. Yao, X. Hou, S. Hu, J. Wang, M. Li, C. Su, M. O. Tade, Z. Shao and X. Liu, Green synthesis of mesoporous  $\text{ZnFe}_2\text{O}_4/\text{C}$  composite microspheres as superior anode materials for lithium-ion batteries, *J. Power Sources*, 2014, **258**, 305–313.
- 30 N. Khadgi, Y. Li, A. Upreti, C. Zhang, W. Zhang, Y. Wang and D. Wang, Enhanced Photocatalytic Degradation of 17 $\alpha$ -Ethinylestradiol Exhibited by Multifunctional  $\text{ZnFe}_2\text{O}_4$ -Ag/rGO Nanocomposite Under Visible Light, *Photochem. Photobiol.*, 2016, **92**, 239.
- 31 J. Feng, Y. Hou, Y. Wang and L. Li, Synthesis of Hierarchical  $\text{ZnFe}_2\text{O}_4@/\text{SiO}_2@/\text{RGO}$  Core-Shell Microspheres for Enhanced Electromagnetic Wave Absorption, *ACS Appl. Mater. Interfaces*, 2017, **9**, 14103–14111.
- 32 Y. Lei, Y. Chen, P. Yu, G. He, Y. Zhu and H. Chen, Combination of  $\alpha\text{-Fe}_2\text{O}_3$ , CdS and reduced graphene oxide: high-performance and recyclable visible light photocatalysis, *Appl. Organomet. Chem.*, 2020, **34**, e5340.
- 33 A. Behera, S. Mansingh, K. Das and K. Parida, Synergistic  $\text{ZnFe}_2\text{O}_4$ -carbon allotropes nanocomposite photocatalyst for norfloxacin degradation and Cr(VI) reduction, *J. Colloid Interface Sci.*, 2019, **544**, 96–111.
- 34 B. Liu, X. Li, Q. Zhao, Y. Hou and G. Chen, Self-templated formation of  $\text{ZnFe}_2\text{O}_4$  double-shelled hollow microspheres for photocatalytic degradation of gaseous *o*-dichlorobenzene, *J. Mater. Chem. A*, 2017, **5**, 8909–8915.
- 35 L. Hou, L. Lian, L. Zhang, G. Pang, C. Yuan and X. Zhang, Self-Sacrifice Template Fabrication of Hierarchical Mesoporous Bi-Component-Active  $\text{ZnO}/\text{ZnFe}_2\text{O}_4$  Sub-Microcubes as Superior Anode Towards High-Performance Lithium-Ion Battery, *Adv. Funct. Mater.*, 2015, **25**, 238–246.
- 36 S. Wang, J. Zhang, J. Yang, X. Gao, H. Zhang, Y. Wang and Z. Zhu, Spinel  $\text{ZnFe}_2\text{O}_4$  nanoparticle-decorated rod-like  $\text{ZnO}$  nanoheterostructures for enhanced gas sensing performances, *RSC Adv.*, 2015, **5**, 10048–10057.
- 37 L. Xu and J. Wang, Magnetic Nanoscaled  $\text{Fe}_3\text{O}_4/\text{CeO}_2$  Composite as an Efficient Fenton-Like Heterogeneous Catalyst for Degradation of 4-Chlorophenol, *Environ. Sci. Technol.*, 2012, **46**, 10145–10153.
- 38 Y. Li, K. Huan, D. Deng, L. Tang, J. Wang and L. Luo, Facile Synthesis of  $\text{ZnMn}_2\text{O}_4@/\text{rGO}$  Microspheres for Ultrasensitive Electrochemical Detection of Hydrogen Peroxide from Human Breast Cancer Cells, *ACS Appl. Mater. Interfaces*, 2012, **12**, 3430–3437.
- 39 J. Luo, Z. Yan, R. Liu, J. Xu and X. Wang, Synthesis and excellent visible light photocatalysis performance of magnetic reduced graphene oxide/ $\text{ZnO}/\text{ZnFe}_2\text{O}_4$  composites, *RSC Adv.*, 2017, **7**, 23246.
- 40 Y. Fu and X. Wang, Magnetically Separable  $\text{ZnFe}_2\text{O}_4$ -Graphene Catalyst and its High Photocatalytic Performance under Visible Light Irradiation, *Ind. Eng. Chem. Res.*, 2011, **50**, 7210–7218.
- 41 D. Yang, J. Feng, L. Jiang, X. Wu, L. Sheng, Y. Jiang, T. Wei and Z. Fan, Photocatalyst Interface Engineering: Spatially Confined Growth of  $\text{ZnFe}_2\text{O}_4$  within Graphene Networks as Excellent Visible-Light-Driven Photocatalysts, *Adv. Funct. Mater.*, 2015, **25**, 7080–7087.
- 42 J. He, Y. Cheng, T. Wang, D. Feng, L. Zheng, D. Shao, W. Wang, W. Wang, F. Lu, H. Dong, R. Zheng and H. Liu, Enhanced photocatalytic performances and magnetic recovery capacity of visible-light-driven Z-scheme  $\text{ZnFe}_2\text{O}_4/\text{AgBr}/\text{Ag}$  photocatalyst, *Appl. Surf. Sci.*, 2018, **440**, 99–106.
- 43 K. Wang, S. Zhan, H. Sun, D. Zhang and J. Wang, Hollow porous core-shell  $\text{ZnFe}_2\text{O}_4/\text{AgCl}$  nanocubes coated with EDTA and Ag nanoparticles for enhanced photocatalytic performances of visible-light-driven, *Chem. Eng. J.*, 2020, **400**, 125908.
- 44 Z. Ji, X. Shen, Y. Song and G. Zhu, In situ synthesis of graphene/cobalt nanocomposites and their magnetic properties, *Mater. Sci. Eng., B*, 2011, **176**, 711–715.
- 45 L. Liu, R. Gao, L. Sun, S. Han, D. Chen, Z. Hua and X. Liu, Ultrahigh cycling stability and rate capability of  $\text{ZnFe}_2\text{O}_4@/\text{graphene}$  hybrid anode prepared through a facile syn-graphenization strategy, *New J. Chem.*, 2016, **40**, 3139–3146.
- 46 T. Li, S. Luo and L. Yang, Microwave-assisted solvothermal synthesis of flower-like  $\text{Ag}/\text{AgBr}/\text{BiOBr}$  microspheres and their high efficient photocatalytic degradation for *p*-nitrophenol, *J. Solid State Chem.*, 2013, **206**, 308–316.
- 47 W. Teng, X. Li, Q. Zhao and G. Chen, Fabrication of  $\text{Ag}/\text{Ag}_3\text{PO}_4/\text{TiO}_2$  heterostructure photoelectrodes for efficient decomposition of 2-chlorophenol under visible light irradiation, *J. Mater. Chem. A*, 2013, **1**, 9060–9068.
- 48 C. Yuan, H. Cao, S. Zhu, H. Hua and L. Hou, Core-shell  $\text{ZnO}/\text{ZnFe}_2\text{O}_4@/\text{C}$  Mesoporous Nanospheres with Enhanced Lithium Storage Properties towards High-performance Li-ion Batteries, *J. Mater. Chem. A*, 2015, **3**, 20389–20398.
- 49 T. Yang, J. Xue, H. Tan, A. Xie, S. Li, W. Yan and Y. Shen, Highly Ordered  $\text{ZnO}/\text{ZnFe}_2\text{O}_4$  Inverse Opals with Binder-free Heterojunction Interfaces for High-performance Photoelectrochemical Water Splitting, *J. Mater. Chem. A*, 2018, **6**, 1210–1218.
- 50 P. Li, Z. Zhou, Q. Wang, M. Guo, S. Chen, J. Low, R. Long, W. Liu, P. Ding, Y. Wu and Y. Xiong, Visible-Light-Driven Nitrogen Fixation Catalyzed by  $\text{Bi}_5\text{O}_7\text{Br}$  Nanostructures: Enhanced Performance by Oxygen Vacancies, *J. Am. Chem. Soc.*, 2020, **142**, 12430–12439.
- 51 H. Chen, W. Liu and Z. Qin,  $\text{ZnO}/\text{ZnFe}_2\text{O}_4$  nanocomposite as a broad-spectrum photo-Fenton like photocatalyst with near-infrared activity, *Catal. Sci. Technol.*, 2017, **1**–3.
- 52 P. Mishra, A. Behera, D. Kandi, S. Ratha and K. Parida, Novel Magnetic Retrievable Visible-Light-Driven Ternary  $\text{Fe}_3\text{O}_4@/\text{NiFe}_2\text{O}_4/\text{Phosphorus-Doped g-C}_3\text{N}_4$  Nanocomposite



- Photocatalyst with Significantly Enhanced Activity through a Double-Z-Scheme System, *Inorg. Chem.*, 2020, **59**, 4255–4272.
- 53 K. Chang, X. Hai, H. Pang, H. Zhang, L. Shi, G. Liu, H. Liu, G. Zhao, M. Li and J. Ye, Targeted Synthesis of 2H- and 1T-Phase MoS<sub>2</sub> Monolayers for Catalytic Hydrogen Evolution, *Adv. Mater.*, 2016, **28**, 10033–10041.
  - 54 L. Yao, N. Guijarro, F. Boudoire, Y. Liu, A. Rahmanudin, R. Wells, A. Sekar, H. Cho, J. Yum, F. Formal and K. Sivula, Establishing Stability in Organic Semiconductor Photocathodes for Solar Hydrogen Production, *J. Am. Chem. Soc.*, 2020, **142**, 7795–7802.
  - 55 H. Zhou, X. Sheng, J. Xiao, Z. Ding, D. Wang, X. Zhang, J. Liu, R. Wu, X. Feng and L. Jiang, Increasing the Efficiency of Photocatalytic Reactions *via* Surface Microenvironment Engineering, *J. Am. Chem. Soc.*, 2020, **142**, 2738–2743.
  - 56 J. Wang, Q. Zhang, F. Deng, X. Luo and D. Dionysiou, Rapid toxicity elimination of organic antibiotics by the photocatalysis of environment-friendly and magnetically recoverable step-scheme SnFe<sub>2</sub>O<sub>4</sub>/ZnFe<sub>2</sub>O<sub>4</sub> nano-heterojunctions, *Chem. Eng. J.*, 2020, **379**, 122264.
  - 57 N. Liang, M. Wang, L. Jin, S. Huang, W. Chen, M. Xu, Q. He, J. Zai, N. Fang and X. Qian, Highly Efficient Ag<sub>2</sub>O/Bi<sub>2</sub>O<sub>2</sub>CO<sub>3</sub> p–n Heterojunction Photocatalysts with Improved Visible-Light Responsive Activity, *ACS Appl. Mater. Interfaces*, 2014, **6**, 11698–11705.
  - 58 M. Vadiyar, S. Kolekar, J. Chang, Z. Ye and A. Ghule, Anchoring Ultrafine ZnFe<sub>2</sub>O<sub>4</sub>/C nanoparticles on 3D ZnFe<sub>2</sub>O<sub>4</sub> nano-flakes for Boosting Cycle Stability and Energy Density of Flexible Asymmetric Supercapacitor, *ACS Appl. Mater. Interfaces*, 2017, **9**, 26016–26028.
  - 59 W. Zhang, A. Mohamed and W. Ong, Z-Scheme Photocatalytic Systems for Carbon Dioxide Reduction: Where Are We Now?, *Angew. Chem., Int. Ed.*, 2020, 22894–22915.
  - 60 Y. Wang, C. Yang, A. Chen, W. Pu and J. Gong, Influence of yolk-shell Au@TiO<sub>2</sub> structure induced photocatalytic activity towards gaseous antibiotic degradation under visible light, *Appl. Catal., B*, 2019, **251**, 57–65.
  - 61 H. Guo, T. Ke, N. Gao, Y. Li and X. Cheng, Enhanced degradation of aqueous norfloxacin and enrofloxacin by UV-activated persulfate: Kinetics, pathways and deactivation, *Chem. Eng. J.*, 2017, **316**, 471–480.

